LA-UR-22-21218

Title: Physics Guided Simulation of Electrostatic Discharge: Technical Report

Author(s):
Pocher, Liam Alexander
Rose, John William
Peery, Travis B.
Mace, Jonathan Lee

Intended for: Report

Issued: 2022-02-11

Los Alamos
NATIONAL LABORATORY

Physics Guided Simulation of Electrostatic Discharge: Technical Report

Liam A. Pocher*†, John W. Rose*‡, Travis B. Peery§, Jonathan L. Mace*
Los Alamos National Laboratory (LANL), Los Alamos, NM
*W-10, LANL
†Department of Physics, University of Maryland
‡Department of Physics, Colorado School of Mines
§T-1, LANL
Emails: liam@lanl.gov ; jrose@lanl.gov ; tpeery@lanl.gov ; jonathan@lanl.gov

CONTENTS

LIST OF FIGURES

LIST OF TABLES

Abstract**—Triboelectrically-charged objects may create threshold sparks, electrostatic discharge (ESD) events, to equilibrate charge between themselves and other relatively charged objects. ESD events exhibit many complex physical phenomena. They are a nexus of several fields of physics with disparate characteristic scales: plasma physics, chemical kinetics, hydrodynamics, circuit models, etc. These scales can span many orders of magnitude from the varied collisions thermalizing information within a plasma on the $\mathcal{O}(fs/ps)$ to the physical size of the plasma channel on the $\mathcal{O}(100\mu m)$, to the speed of a nonlinear hydrodynamic wave propagating at $\mathcal{O}(\mu m, ns)$. These threshold ESD events may occur in situations of programmatic importance, delivering energy and power profiles to a "victim load" generating deleterious consequences. To predict and mitigate these consequences we must answer questions about the spark's energy budget: how much energy goes into producing the spark channel; how much gets radiated away; how much energy is advected away into the hydrodynamics; and how much energy is delivered to a victim load. An ESD simulation toolset has been created and evolved in order to answer these questions. An appropriate, physics-guided implementation for simulation can be done by gaining insight into its constituent physics and leveraging that intuition to choose a suitable numerical operator. We examine in detail the chemical kinetics, circuit discharge, and hydrodynamics to determine dominant regimes, values, timescales, and interactions to uncover the underlying physical dynamics. We also examine and propose model reduction schemes for high-dimensional chemical kinetics. We use past and current work with experimentally-validated and theoretically-verified hydrodynamics to calculate applicability limits of the non-ionizing strong shock limit. We quantify the energy budget from a hydrodynamic perspective and demonstrate that a significant fraction of the stored energy is "earmarked" for hydrodynamic advection as an energy terminus. Lastly, we combine the constituent physics of an ESD event (chemical kinetics, circuit model, and hydrodynamics) into a cohesive, actionable toolset and obtain promising results from an isothermal test case. We then propose a viable, modular evolution of the ESD toolset based upon the performed examination of the physics uncovering dominant physical scales and the stiffness of the compositional differential system.**

I. INTRODUCTION

Threshold electrostatic discharge (ESD) events (sparks) are a nexus of the fields of hydrodynamics, chemical kinetics, plasma physics, electromagneism, and statistical mechanics, see Fig. 1. There has been a large effort the past five years at both the Colorado School of Mines (CSM) [1], [2], [3], [4], [5], [6], [7], [8], [9], [10], [11], and at Los Alamos National Laboratory [12], [13], [14], [15], [16], [17], [18], [19], [20] to describe these threshold sparks. These efforts have spanned theoretical work done by David Flammer solving the electron distribution function, numerical work modeling the spark gap breakdown and streamer propagation by John Rose, and experimental efforts producing sparks in air and other gases by Charles "Chip" Durfee and his students. The work documented within this report fits within the larger whole by combining some of the constituent physics of ESD events into an ESD simulation capability. This is accomplished by looking at the requisite physical scales, examining in detail the dominant physics and using that gleaned insight to eventually propose a suitable numerical operator motivated by physics.

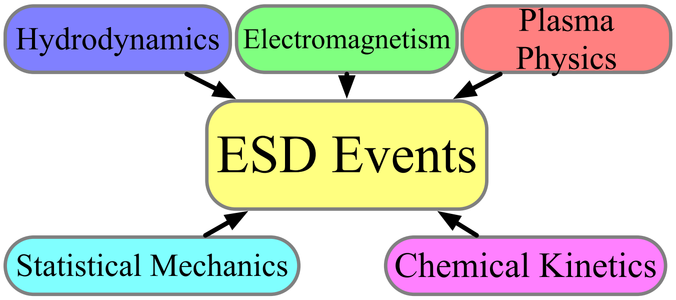

Fig. 1: ESD events are a nexus of many fields of physics: electromagnetism, fluid dynamics, chemical kinetics, statistical mechanics, and plasma physics. It takes tools from all of these fields in order to be successful in the ESD Initiative.

The Laboratory's stockpile stewardship mission is predicated upon a holistic marriage of experimental, computational, and theoretical physics, Fig. 2. This holistic marriage of disciplines is a common theme in physics. The combination of all three is greater than individual sums of their parts, enabling guarantees and enforcement.

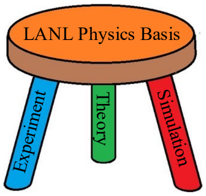

Fig. 2: Cartoon schematic of how the laboratory's mission is predicted upon the marriage of experimental, computational, and theoretical physics. The ESD simulation toolset will be an integration of all these disciplines into a synergized whole.

Simulation has had increasing visibility in recent decades for well-known and documented reasons. In this report we document the integration of finite element hydrodynamic, plasma chemistry and circuit models into a cohesive, actionable package. Electromagnetism is not considered on these timescales due to the speed that which electromagnetic radiation propagates*. Statistical mechanics is implicitly considered due to the hydrodynamic equations (Euler or Navier-Stokes) being moments of the Boltzmann equation which comes from the BBGKY hierarchy underpinning much of classical field theory when applied to statistical mechanics†. The simulations are done to enumerate and then quantify the possible energy flow pathways in the complex energy network that are ESD events, Fig. 3. The beginning node, green circle, of this energy pathway is energy stored on the charged object. One energy terminus, red circle, is the energy going into shock formation and resultant hydrodynamic propagation. This detailed analysis by simulation is being performed because we are *obligated* to get the right answer for the right reasons to avoid deleterious consequences for detonator safety.

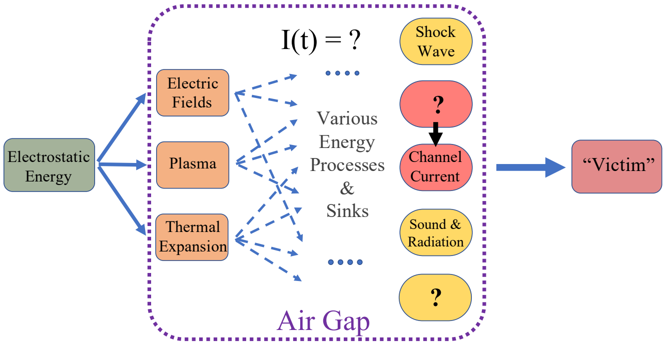

Fig. 3: ESD events constitute a complex network of pathways for energy to go down in a cascade from being stored initially on a charged object to any number of terminuses.

Deleterious consequences stemming from detonator are causes for concern along an axis of acceptable probable events. One physical mechanism in ESD events that causes concern is a possible positive feedback cycle, Fig. 4, whereby expansion caused by an increase in the thermodynamic equation of state (pressure) causes advection and thus a decrease in mass density ρ along the axis of symmetry $r = 0$ of a cylindrical channel used to model the ESD event. The density decrease along the axis of symmetry then causes characteristic plasma variables (reduced electric field, ionization rate, drift velocity etc.) to increase thusly increasing the channel current I and increasing the energy deposited into the channel q_0. It is thought that this increased energy deposition causes further increase of the thermodynamic pressure, perpetuating the cycle beginning with hydrodynamic advection. By performing this simulation work we believe that by including physically motivated and appropriate constituent physics (hydrodynamic, plasma kinetic, and circuit) we obtain the *right* answer for the *right* reasons.

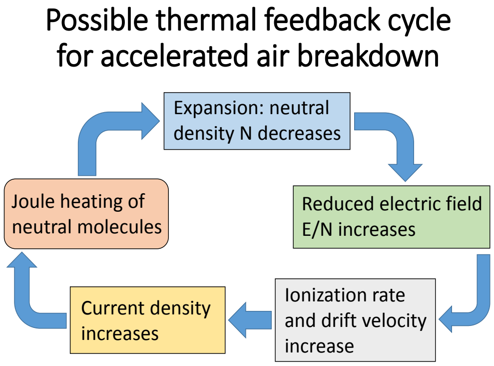

Fig. 4: ESD events may possibly have the positive feedback cycle involving hydrodynamic evolution of the neutral number density along the axis of symmetry, plasma variables, and joule heating.

This content of the report is as follows. Section II provides an overview of the utilized finite element hydrodynamic solver. Section III provides a detailed analysis of the chemical kinetics constituting this differential system that is part of the total system solved on a cell-by-cell basis within the hydrodynamic code. Section IV provides an analysis into reduction methods from three perspectives: dynamical systems and differential geometry (slow manifolds), statistical physics, and data science. Section V provides an overview of some past and current work done by the authors from a hydrodynamic perspective with a hydrodynamic simulation. This includes simulation validation and verification of a simulation suite using the described finite element code. Finally, Section VI discusses the conclusions to be gained from the work documented within this report.

II. COMPUTATIONAL SIMULATIONS

Physics is dominated by physical scales (time, energy, velocity, length, charge, etc.). One wouldn't model the sun with ambient room temperature and pressure conditions, nor would one model a shockwave with incompressible fluid flow. In our choice of numerical software/operator we have let the physics drive us. In our plasma kinetic model for example there are (1) sensitive dominant species, $N_\alpha^{(dom)}/\eta_\alpha^{(dom)}$ with N being the species number and η being the log10 of that species number ($\eta_\alpha \equiv N_{(\alpha)}$) (2) dominant timescales $\tau^{(dom)}$ and (3) dominant interaction between species (how do species grow and decay as a function of time?). The dominant scales that we have uncovered with this analysis have helped us form the recommendation for a viable, modular evolution of the ESD simulation toolset.

The hydrodynamics that are part of ESD events exhibit nonlinear hydrodynamic waves. There are a multitude of hydrodynamic solvers existing at LANL. We have chosen to use Fierro [21], [22] with which we have performed past work

---

[*] The speed of light $c \sim$ 3e8 m/s≈ft/ns is much greater than than the timescale of interest in our simulations which are on the order of µm/ns.

[†] We implicitly assume that the distribution of velocities in each and every individual cell in our hydrodynamic simulation follows a Maxwell-Boltzmann distribution (Gaussian $\sim e^{-(v-v_{stream})^2}$). Each cell must satisfy the competing conditions of having enough particles to be statistically representative, and be small enough that thermodynamic variables may be accurately approximated as homogenous throughout.

[12], [13]. Fierro is an Arbitrary Lagrangian Eulerian (ALE) code. We have used solely the Lagrangian capability of Fierro, see Figs. 5 and 6 for a schematic showcasing the difference between Eulerian and Lagrangian codes and ALE.

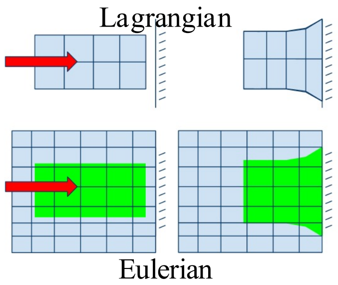

Fig. 5: Cartoon schematic of Eulerian versus Lagrangian perspectives for tracking material with the fluid dynamic conservation equations. Schematic courtesy of Donald "Trip" Haynes. The green blob in the lower part of the figure is what the light blue Lagrangian code would be in the Eulerian description.

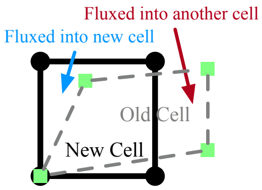

Fig. 6: A schematic showing how material is fluxed into one cell or another in the Arbitrary Lagrangian Eulerian (ALE) algorithm.

The geometry of the simulations we are considering is shown in Fig. 7 and Fig. 8. The purple volumes approximate the domain of an ESD event in our simulations.

Figure 7 shows the effective domain in our simulations with the purple rectangular prism which is one cell thick in the z direction, and is bounded by the $y-z$ plane at $x=0$ and the $x-z$ plane at $y=0$. The grey boundary wall represents a reflecting boundary conditions at the domain edge. Our simulations model a cylindrical ESD event occurring at the center of an infinitely long, hollow, perfectly reflecting rectangular prism. The blue cylinder is an approximation for the spark channel, with the yellow object signifying the spark event.

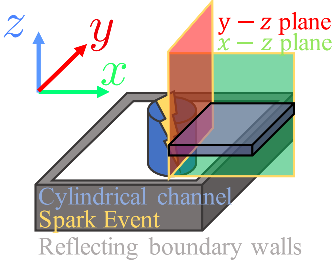

Fig. 7: Cartoon schematic of the ESD simulations.

Figure 8 shows the cylindrical spark channel in more detail. We assume that the spark channel obeys both axial symmetry in z (T_z) and rotation symmetry ϕ in the $x-y$ plane $(SO(2))$ about the axis of symmetry. The white text shows the "pie slice" that our simulation domain approximates in cylindrical geometry bounded by the green and red lines of the x and y coordinate axes. The yellow arrow shows the radial direction. This figure also shows the purple simulation domain to be one cell thick, approximating axial symmetry, in our inherently 3D hydrodynamic code.

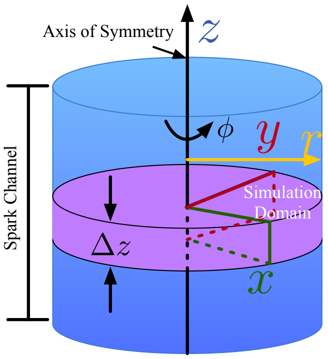

Fig. 8: Cylinder schematic of the ESD simulation.

In our prior work examining hydrodynamics arising from ESD events we noted three distinct regimes, Fig. 9: expanded cells whose center of mass advected away from the axis of symmetry, compressed cells near and right behind the shock, and finally the undisturbed mesh simulating quiescent material. These flow regimes occurred at later times after a nonlinear hydrodynamic wave propagated away from the axis of symmetry. These regimes of flow have analogues in other experimental and numerical studies that study hydrodynamic advection [23], [24], [25].

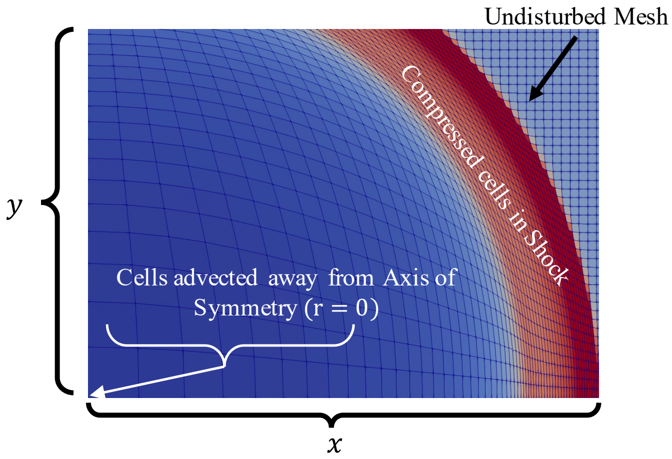

Fig. 9: Sample simulation result with distinct, annotated regimes of flow at at specific instant of time. The cylinder axis, spark axis $\hat{z}$, is coming out of the page toward the reader.

To conclude this section we would like to state that the combination of the plasma kinetics, circuit, and hydrodynamic models is not a magnetohydrodynamic (MHD) simulation.

MHD simulations are inherently non causal due to their ignoring of eddy currents in Maxwell's equations. We wish to obtain the *right* answer for the *right* reasons to obtain insight regarding dominant physics inherent within ESD events that contribute to various energy terminuses with our current combination of physics.

III. PHYSICAL ANALYSIS

The constituent physics of ESD events have physical scales that span orders of magnitude from ps to ms and from nm to mm. In this section we delve into the deeper details of the plasma kinetics, the fastest timescale physics within threshold sparks, in order to glean insight into what numerical operator is appropriate. This will be done by: analyzing dominant species $N^{(dom)}/\eta^{(dom)}$ at equilibrium for fixed electron temperature kT_e; timescales of equilibration $\tau_{(eq)}$; and interactions from a Jacobian matrix (to be described later).

A. Chemical Kinetics

This section was excerpted and adapted from an unpublished report, "Electrostatic Discharge Physics," by John W. Rose, Claudia A. M. Schrama, Sarah C. Hinnegan, Jonathan Barolak, Forrest Doherty, Daniel E. Adams, P. David Flammer, and Charles G. Durfee (Colorado School of Mines, 2020).

1) ESD: Introduction, Definitions, and Assumptions: Electrostatic discharge (ESD) is the rapid ($\leq$ µs timescale) neutralization of charge between two statically-charged objects in close proximity. ESD begins with the electrical breakdown of the air gap between objects, resulting in the formation of a conductive, transient plasma filament (spark) that bridges the gap. Fast current pulses from ESD represent a threat to sensitive devices such as explosive detonators due to the possibility of rapid energy deposition.

a) Discharge current and victim load: Here the sensitive device in question is abstractly represented as a resistive "victim" load in a circuit. The energy dissipated in the victim, $\mathcal{E}_v$, is found as a function of time t via

$$\mathcal{E}_v(t) = \int_0^t I(t')^2 R_v \, dt',$$

where the resistance R_v is assumed to be a constant property of the victim. If $\mathcal{E}_v(t)$ exceeds critical values within a certain duration, the victim can experience an adverse response. Therefore, the time-dependent current $I(t)$ is a key quantity of interest for the CSM-LANL ESD initiative.

b) Circuit Models: The charged objects constituting the ESD system are assumed to be represented as circuit elements by a capacitance C and an inductance L. In the worst case, the victim R_v is in series with these elements and the time-dependent spark resistance $R_s(t)$. This circuit is depicted in Fig. 10 and is an applicable model when the discharge occurs between two conducting surfaces (electrodes). Although this circuit can be written as a 2nd order ODE for the capacitor charge $Q(t)$, it can be more convenient to write it as a coupled system of 1st order equations for $I(t)$ and $Q(t)$,

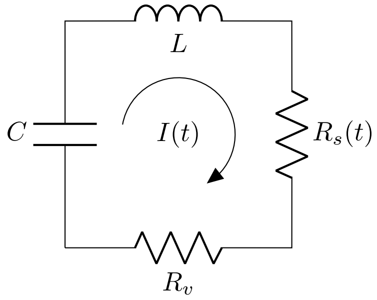

Fig. 10: Simple circuit model of ESD.

$$\frac{dQ}{dt} = -I \tag{1}$$

$$L\frac{dI}{dt} = -(R_s + R_v)I + \frac{Q}{C}, \tag{2}$$

subject to the initial conditions $I(0) = 0$ and $Q(0) = CV_0$, where V_0 is the initial voltage across the capacitor. The initial stored energy in the circuit is $\mathcal{E}_0 = CV_0^2/2$, and thus the ESD problem can be restated as finding the fraction of $\mathcal{E}_0$ that constitutes $\mathcal{E}_v$, with the remainder dissipated in the spark through $R_s(t)$.

c) Spark Resistance: Here we assume the spark gap geometry approximates parallel plate electrodes with a uniform electric field of magnitude E. The spark channel is taken to be a cylindrical filament with uniform properties over its volume $\mathcal{V}$, shown in Fig. 11, with a fixed gap spacing of z_s. The spark radius $r_s(t)$ is generally a function of time and increases due to gas heating and expansion. Because the electromagnetic skin depth of the spark plasma is large relative to typical values of r_s, the electric field E from the electrodes is not screened within the spark channel [26]. With an axially-uniform cross section of $\mathcal{A}_s = \pi r_s^2$, the spark resistance R_s is [27]

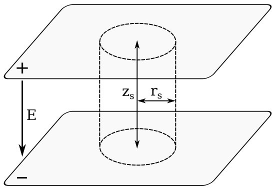

Fig. 11: Geometry of idealized cylindrical spark channel between parallel plate electrodes. Spark radius r_s has been exaggerated relative to electrode spacing z_s for clarity (typically $r_s \ll z_s$).

$$R_s = \frac{z_s}{\mathcal{A}_s \sigma} = \frac{z_s}{\pi r_s(t)^2 \sigma} \approx \frac{z_s}{\pi r_s(t)^2 e n_e \mu_e}, \tag{3}$$

where σ is the electrical conductivity of the spark plasma. Because the electron mobility μ_e typically exceeds the ion mobility by roughly two orders of magnitude [28], the conductivity can be approximated as $\sigma \approx e n_e \mu_e$, where e is the magnitude of the electron charge and n_e is the electron number density. n_e is related to the total number N_e of electrons in the channel as $n_e = N_e/\mathcal{V}$.

2) Kinetic Model and Equation System: Rather than start with the molecular species of air with their more complex kinetic processes, the focus here was on analyzing sparks in a pure monatomic gas for simplicity. Atomic hydrogen was chosen for its simple energy level structure and the availability of cross section data for electron scattering. The reactions considered in the model included:

- Elastic collisions: $e + \mathrm{H}(n) \rightleftharpoons e + \mathrm{H}(n)$
- Ionization/3-body recombination: $e + \mathrm{H}(n) \rightleftharpoons e + e + \mathrm{H}^+$
- Excitation/de-excitation: $e + \mathrm{H}(n) \rightleftharpoons e + \mathrm{H}(n+1)$
- Spontaneous line emission: $\mathrm{H}(n+1) \to \mathrm{H}(n) + \hbar\omega_{ph}$
- Radiative recombination: $e + \mathrm{H}^+ \to \mathrm{H}(n) + \hbar\omega_{ph}$

where $n = 1, 2, 3, \ldots, n_{\text{max}}$ is the principal quantum number. The value n_{max} is a cutoff to the higher excited states attainable by an atom due to the presence of nearby atoms in the gas — in other words, the volume available to the electron orbital is finite. The ionization cross sections were calculated for arbitrary n using the formula of Vriens and Smeets [29], while the excitation cross sections for transitions $n \to n'$, with $n' > n$, were taken from the formulae of L. C. Johnson [30]. Although more recent data are available, these cross sections were chosen for their simple analytical forms that facilitated computation of closed expressions for the rate coefficients. Cross sections for radiative recombination and Einstein A_{ij} coefficients for spontaneous emission were taken from semi-classical formulae in Raizer and Zel'dovich's book [31].

For binary collisions (e.g. ionization, excitation, and radiative recombination), the rate coefficients K_{ij} and A^r_{ij} (for radiative recombination) were calculated assuming a Maxwellian electron energy distribution function (EEDF),

$$\begin{aligned} K_{ij}(k_B T_e) &= \int_0^\infty v(\varepsilon)\sigma_{ij}(\varepsilon)\varepsilon^{1/2} f(\varepsilon)\, d\varepsilon \\ &= \sqrt{\frac{2}{m_e}} \int_0^\infty \varepsilon\sigma_{ij}(\varepsilon) f(\varepsilon)\, d\varepsilon \\ f(\varepsilon) &= \frac{2}{\sqrt{\pi (k_B T_e)^3}} \exp\left(-\frac{\varepsilon}{k_B T_e}\right), \end{aligned} \tag{4}$$

where the EEDF has been normalized as $\int_0^\infty \varepsilon^{1/2} f(\varepsilon)\, d\varepsilon = 1$. Here i and j denote the initial and final state of the atom, respectively, with values $i = 1, 2, \ldots, \mathcal{N} = n_{\text{max}} + 1$ corresponding to $\mathrm{H}(1), \mathrm{H}(2), \ldots, \mathrm{H}(n_{\text{max}}), \mathrm{H}^+$. The 3-body recombination rates K^r_{ij} and de-excitation rates were calculated using the principle of detailed balance (see Appendix for details).

Defining the $\mathcal{N} \times \mathcal{N}$ collisional frequency matrix $\boldsymbol{\nu}$ as

$$\nu_{ij} = \begin{cases} K_{ji} n_e, & i \neq j \neq \mathcal{N} \\ K^r_{ji} n_e^2, & i \neq j = \mathcal{N} \\ -\sum_{k \neq j} \nu_{kj}, & i = j \end{cases}$$

and an $\mathcal{N} \times \mathcal{N}$ matrix $\boldsymbol{a}$ for the emission coefficients,

$$a_{ij} = \begin{cases} A_{ji}, & i < j \neq \mathcal{N} \\ A^r_{ji} n_e, & i < j = \mathcal{N} \\ -\sum_{k \neq j} a_{kj}, & i = j \\ 0, & i > j \end{cases},$$

the rate equation system for the numbers of atoms in each state, vectorially denoted as $\underline{N} = [N_1\ N_2\ N_3\ \ldots\ N_{\mathcal{N}}]^{\mathrm{T}}$, can be written as

$$\frac{d}{dt}\underline{N} = \boldsymbol{\nu}\underline{N} + \boldsymbol{a}\underline{N}. \tag{5}$$

(Alternative notation used in subsequent plots: $\underline{N} = [N_1\ N_2\ N_3\ \ldots\ N_i]^{\mathrm{T}}$ where $N_{\mathcal{N}} = N_i$ is the total ion number.) For the emission processes, the plasma is assumed to be completely optically thin so that the elements below the diagonal in $\boldsymbol{a}$ are zero (no absorption).

Defining $N_0 = \sum \underline{N} = \sum_{j=1}^{\mathcal{N}} N_j$ as the total heavy species number, we see that by taking $\boldsymbol{\nu}$ and summing its columns, we obtain $dN_0/dt = 0$. In other words, N_0 is a constant because the number of nuclei is conserved — atoms can only change their ionization stage, not their nuclear state, based on the reactions considered here. (Recall we are considering "low-temperature" $\sim$ eV plasmas here.)

As a concrete example, consider a model with $n_{\text{max}} = 2$, resulting in $\mathcal{N} = 3$ states (1: ground H(1), 2: excited H(2), 3 or i: ionized H^+). Equation (5) can be written element-by-element in this case as

$$\begin{aligned} \frac{d}{dt}\begin{pmatrix} N_1 \\ N_2 \\ N_i \end{pmatrix} &= \begin{pmatrix} -(K_{12} + K_{1i})n_e & K_{21} n_e & K^r_{i1} n_e^2 \\ K_{12} n_e & -(K_{21} + K_{2i})n_e & K^r_{i2} n_e^2 \\ K_{1i} n_e & K_{2i} n_e & -(K^r_{i1} + K^r_{i2})n_e^2 \end{pmatrix} \begin{pmatrix} N_1 \\ N_2 \\ N_i \end{pmatrix} \\ &+ \begin{pmatrix} 0 & A_{21} & A^r_{i1} n_e \\ 0 & -A_{21} & A^r_{i2} n_e \\ 0 & 0 & -\left(A^r_{i1} + A^r_{i2}\right) n_e \end{pmatrix} \begin{pmatrix} N_1 \\ N_2 \\ N_i \end{pmatrix} \end{aligned}$$

where $N_3 = N_i$ is the total ion number and the K_{ij}, K^r_{ij}, and A^r_{ij} coefficients are generally functions of electron temperature T_e or the EEDF. For the condition of quasi-neutrality,

$$N_i = N_e = n_e \mathcal{V}. \tag{6}$$

a) Energy equations for electrons and heavy species: In general, the electron and heavy species temperatures, T_e and T_g respectively, vary as a function of time due to energy transfer processes in the plasma. In turn, the rates of excitation, ionization, and recombination will also vary in time as the spark develops. To find the time dependence of these temperatures, energy conservation equations for the electrons and heavy species can be formulated and solved simultaneously with the level population equations (5). Taking the channel volume $\mathcal{V} = \pi r_s^2 z_s$ to have spatially-uniform properties, the overall time-dependent energy balance for the spark is

$$\frac{d\mathcal{E}}{dt} = \frac{d\mathcal{Q}}{dt} - P\frac{d\mathcal{V}}{dt},$$

where $\mathcal{E}$ is the total internal energy, $\mathcal{Q}$ is the net heat source, and $Pd\mathcal{V}/dt$ is the work done by the channel when expanding into its surroundings. P is defined here as the total pressure exerted by the channel on its surroundings. For a plasma consisting of electrons and monatomic heavy species, $\mathcal{E}$ is taken to have only the translational degrees of freedom, $\mathcal{E} = (3/2)Nk_BT$, where $N = N_0 + N_e$ is the total number of particles. The electronic excitation of the atoms and ions is accounted for in the population equations (5), so $\mathcal{E}$ doesn't include this degree of freedom. However, electron-atom collisions make a contribution to the heat source $d\mathcal{Q}/dt$. Here, the possibility that electrons may have a different temperature from the heavy species — due to disparities in energy transfer during elastic collisions between electrons and atoms — calls for the use of separate energy equations,

$$\frac{d}{dt}\left(\frac{3}{2}N_e k_B T_e\right) = I^2 R_s - \dot{\mathcal{Q}}_{in} - \dot{\mathcal{Q}}_m - \dot{\mathcal{Q}}_{fb} - P_e\frac{d\mathcal{V}}{dt} \quad (7)$$

$$\frac{d}{dt}\left(\frac{3}{2}N_0 k_B T_g\right) = \dot{\mathcal{Q}}_m - P_g\frac{d\mathcal{V}}{dt}, \quad (8)$$

where N_e is the total number of free electrons, N_0 is the total number of atoms and ions, P_e is the electron pressure, and P_g is the gas pressure (with total $P = P_e + P_g$). $\dot{\mathcal{Q}}_{in}$ and $\dot{\mathcal{Q}}_m$ are power source/sink terms for inelastic and momentum transfer collisions, respectively. To simplify calculations, the $\mathcal{N} \times \mathcal{N}$ transition energy matrix $\mathfrak{E}$ is defined as

$$\mathfrak{E}_{ij} = \begin{cases} \varepsilon_{\mathrm{H}}/i^2, & i < j = \mathcal{N} \\ \varepsilon_{\mathrm{H}}(1/i^2 - 1/j^2), & i < j < \mathcal{N} \\ 0, & i = j \\ -\mathfrak{E}_{ji}, & i > j \end{cases}$$

where $\varepsilon_{\mathrm{H}} \approx 13.6057$ eV is the Rydberg energy. As an example, for $\mathcal{N} = 3$ states $\mathfrak{E}$ is written explicitly as

$$\mathfrak{E}(\mathcal{N} = 3) = \begin{pmatrix} 0 & 3\varepsilon_{\mathrm{H}}/4 & \varepsilon_{\mathrm{H}} \\ -3\varepsilon_{\mathrm{H}}/4 & 0 & \varepsilon_{\mathrm{H}}/4 \\ -\varepsilon_{\mathrm{H}} & -\varepsilon_{\mathrm{H}}/4 & 0 \end{pmatrix}.$$

Using the element-wise (Hadamard) product $\odot$, the terms $\dot{\mathcal{Q}}_{in}$ and $\dot{\mathcal{Q}}_m$ have the form [32],

$$\dot{\mathcal{Q}}_{in} = -\sum_{i=1}^{\mathcal{N}}\sum_{j=1}^{\mathcal{N}} \mathfrak{E}_{ij}\nu_{ij}N_i = -\sum\left(\left(\mathfrak{E}\odot\boldsymbol{\nu}\right)\underline{N}\right) \quad (9)$$

$$\dot{\mathcal{Q}}_m = \frac{2m_e}{M}\nu_m N_e\left(\frac{3}{2}k_BT_e - \frac{3}{2}k_BT_g\right) \quad (10)$$

$$= \frac{3m_e}{M}\nu_m N_e\left(k_BT_e - k_BT_g\right), \quad (11)$$

where m_e is the electron mass and M the atom mass, which is nearly identical between neutrals and ions. In $\dot{\mathcal{Q}}_m$, the smallness of the momentum transfer fraction $2m_e/M$ is one reason why $T_e \gg T_g$ unless $\nu_m N_e$ becomes large (e.g. near full ionization). The method for calculating the momentum transfer collision frequency ν_m is discussed in the Appendix.

The term $\dot{\mathcal{Q}}_{fb}$ in (7) denotes power loss by the electrons due to free-bound (radiative recombination) processes. This has the form

$$\dot{\mathcal{Q}}_{fb} = \sum_{n=1}^{n_{\max}} \dot{\mathcal{Q}}_{fb,n}$$

$$= \frac{N_eN_i}{\mathcal{V}}\sum_{n=1}^{n_{\max}}\int_0^\infty \underbrace{\left(\varepsilon + \varepsilon_{\mathrm{ion},n}\right)}_{\text{photon energy}} v(\varepsilon)\sigma_{\mathrm{rr},n}(\varepsilon)\varepsilon^{1/2}f(\varepsilon)\,d\varepsilon, \quad (12)$$

where $\varepsilon_{\mathrm{ion},n} = \varepsilon_{\mathrm{H}}/n^2$ is the ionization energy from level n and $\sigma_{\mathrm{rr},n}$ is the radiative recombination cross section to level n. In general, there are also free-free transitions (e.g. electron-ion bremsstrahlung) with an associated loss term $\dot{\mathcal{Q}}_{ff}$ in the electron energy equation (7). However, for $k_BT_e \ll \varepsilon_{\mathrm{ion},1} = \varepsilon_{\mathrm{H}}$, typical for plasma conditions considered here, the energy loss to radiative recombination greatly exceeds the bremsstrahlung losses [31]. Therefore, $\dot{\mathcal{Q}}_{ff}$ is neglected in subsequent calculations.

In deriving equations (7) and (8), it has been assumed that the neutral atoms and ions thermally equilibrate rapidly through elastic collisions and thus share a common temperature. Also, the Joule heating term I^2R_s is present in only (7) because (3) makes the approximation that electrons are the predominate contributor to the electrical conductivity.

B. Dominant Species: Critical Points

The chemical kinetics differential system described in Section III-A is a set of coupled first differential equations with $n_s = \mathcal{N}$ equations. There are certain common features that nonlinear differential systems have in common: critical points; critical point stability (neutral, saddle, stable, unstable); composition space Γ_C flow; basins of attraction; etc. There are two consideration that restrict physically allowable solutions in this composition space Γ_C: conservation of species number ($\sum_{\alpha=1}^{n_s} N_\alpha = N_0$ with N_0 being the total number of particles) which projects n_s dimensional species dynamics onto an $n_s - 1$ dimensional manifold; and positive, real number values. Within this allowable Γ_C there exist only two critical points that we have numerically found while fixing electron temperature kT_e (in units of eV), volume V, and applied electric field $\vec{E}$. These two *fixed points* correspond to an unstable source (repeller) whose equilibrium value contains has only nonzero species amount in the ground species i.e. $\vec{N}^{(eq)} = \{N_0, 0, 0, ..., 0\}$ ($N_\alpha^{(eq)} = 0$ for $\alpha \neq 1$) and a stable sink (attractor) with finite values of species number in all the species populations i.e. $N_\alpha^{(eq)} \neq 0$. The basin of attraction of the stable sink is all allowable composition space Γ_C, except for the unstable source which is a set of Lebesgue measure zero in the $n_s - 1$ dimensional space.

We may intuitively think of these two allowable critical points as being on top of windy mountain ready to tip over at any moment (unstable source), or being in the middle of deep valley (stable sink), see Fig. 12. To mathematically find the critical points of the n_s dimensional chemical kinetic differential system ($n_s \in \{3, 4, 10\}$) we may set the evolution equations detailed in Section III-A equal to zero. This may be written as

$$\left.\frac{d\vec{N}}{dt}\right|_{\vec{N}^{(eq)}} = \vec{0}\,. \tag{13}$$

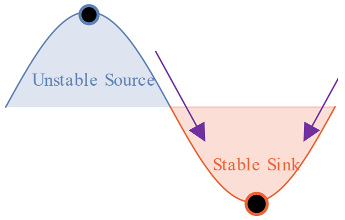

Fig. 12: Critical points cartoon.

Plots of the solutions to these differential equations as a function of *fixed* electron temperature kT_e where k is Boltzmann's constant and and T_e the actual temperature of the electrons may be seen in Fig. 13. Figures 13a to 13d shows the solutions to Eq. (13) for n_s equaling 3, 4, 10, and a zoomed plot of n_s equaling 10, respectively. For low temperature the ground species N_1 dominates while at higher temperature (> 2 eV) the ionized state N_i dominates. Consistently within these plots we may observe that between 1 and 2 eV the dominant species at equilibrium switches from ground to ionized. An interesting thing to note, though, is the behavior of the excited states as more and more species are included within the model. For moderate electron temperatures ($\approx 2 - 4$ eV) the excited states have a non-insignificant amount of the conserved total population number within the differential system and they "eat away" at the total dominance of the equilibrium ionized species number $N_i^{(eq)}$. However, as before with the ground species, at higher electron temperatures they too begin to erode away and the ionized species recovered its dominance.

With the dominant equilibrium species populations found for a fixed electron temperature, volume, and applied electric field we may begin to ask the questions as to what changes once temporal dynamics and interactions are allowed. To further analyze our constructed differential system, we may quantify how long it takes for an individual system to reach this equilibrium for fixed electron temperature, and how it gets there.

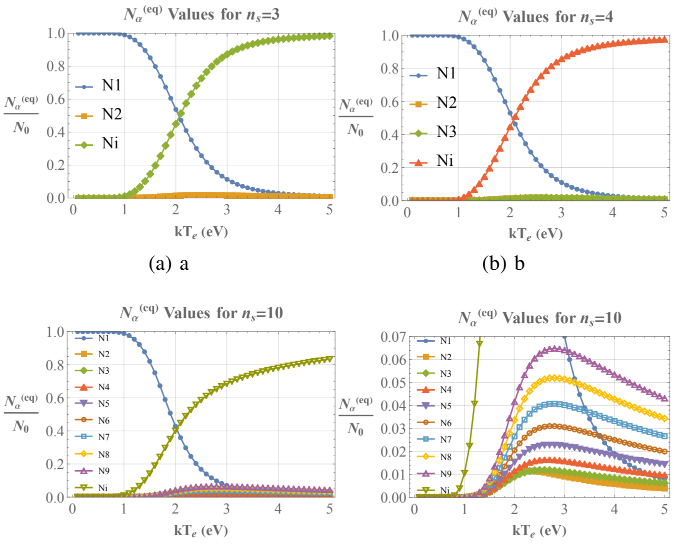

(a) a (b) b

(c) c (d) d

Fig. 13: Critical points found from the chemical kinetic differential system used within this work.

C. Dominant Timescales: Lyapunov Functions

To more readily answer the question of how long it takes to get from the mountaintop to the valley we perform a change of variables to better visualize the dynamics inherent within this complex, interwoven differential system. As scientists and engineers, we prefer simpler, less complicated answers than convoluted ones! Oftentimes this boils down to performing a rescaling such that the observed relationships are no longer complicated but linear. To place our species compositions into a linear space we take a log base 10 transformation

$$\eta_\alpha \equiv \log_{10}(N_\alpha) \;\; \text{s.t.} \;\; \eta_\alpha \in \{\eta_1, \eta_2, ..., \eta_{n_s}\}\,.$$

with η_α being the corresponding exponent 10 would have to be raised to obtain N_α. With these new variables we may define a normalized positive definite distance function called a Lyapunov function $V_{\vec{\eta}}$ [33]. The functional form of this Lyapunov function

$$V_{\vec{\eta}}(t; \vec{\eta}) = \frac{1}{\eta_0}\sqrt{\frac{1}{n_s}\sum_{\alpha=1}^{n_s}\left(\eta_\alpha(t) - \eta_\alpha^{(\text{eq})}\right)^2} \tag{14}$$

with $V_{\vec{\eta}}$ being the scalar output of the Lyapunov function, t being the time the Lyapunov function is evaluated at, $\vec{\eta}$ being the n_s dimensional vector that is input into the Lyapunov function, $\eta_0 \equiv \log_{10} N_0$ being the normalized base 10 logarithm of the ambient species number, $\eta_\alpha^{(eq)}$ the equilibrium population of species η_α, and the the root mean square operation a positive Euclidean distance metric $|\vec{\eta}(t) - \vec{\eta}^{(eq)}|$. This function calculates the normalized distance away from equilibrium.

Near equilibrium many systems may be treated as linear and thusly we perform a linearization of the solution space near a critical points to determine its stability. Because the critical point $\vec{\eta}^{(eq)}$ is stable, we may we treat the solution as asymptotically approaching the fixed points. Due to this asymptotic nature, the solution will never mathematically reach the critical point, but will computationally due to underflow and round off error. To avoid such issues, we stipulate a minimum small distance in the normalized space ε that once the Lyapunov function has reached within we consider the solution to have reached equilibrium. We call the time for this to occur the equilibration time τ^{eq}. Mathematically this is

$$V_{\vec{\eta}}(t;\vec{\eta}) < \underbrace{\varepsilon}_{\text{small}} \Rightarrow \boxed{t \equiv \tau^{(\text{eq})}}.$$

A visual cue for this occurring is Fig. 14 which shows the system equilibrium point, $\vec{\eta}^{(eq)}$, being a rabbit that is tied down or not depending on whether we fix the electron temperature for the simulation. The system state may be thought of a dog chasing this rabbit. Once the dog is within a hypersphere of radius ε then the dog would be considered to have caught the rabbit. The system will have equilibrated (asymptotically)!

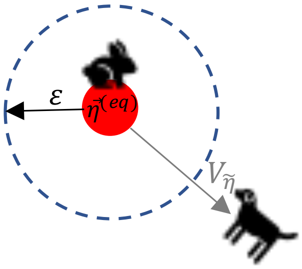

Fig. 14: Lyapunov Exponent visualization.

Continuing using the differential systems analyzed in Section III-B we calculate both the Lyapunov function for varied electron temperature, Fig. 15, and the equilibration times $\tau^{(eq)}$, Fig. 16. Figures 15a to 15c show how as the electron temperature kT_e is increased the sudden and rapid falloff for the Lyapunov function. For most of the simulation in the log-linear plot, we observe four distinct, sequential behavior regimes:

1) Initial decrease from the initial condition's value
2) Approximately constant $V_{\vec{\eta}}(t)$
3) Rapid fall of Lyapunov function $V_{\vec{\eta}}(t)$
4) Numerical noise from the software shown in the purple box

From Figs. 15a to 15c we excise the location where the Lyapunov function is less than $\varepsilon = 1.0e{-}7$. The results of this are shown in Fig. 16. A log-log plot was not used due to the lack of decades of electron temperature kT_e dynamics/data. Note that as we vary the n_s dimension of the composition space Γ_C the overall structure of the line doesn't change that much. The discrete jumps/hops in the lower right of the plot at from the discrete nature of the time step used[‡]. The major takeaways from this plot are the disparate times with which the system (dog) takes to asymptotically equilibrate to the *fixed* equilibrium solution $\vec{\eta}^{(eq)}$ (rabbit). For "low" temperatures (< 1.5 eV which is the majority of the numerical in our simulations), the system takes over a microsecond to equilibrate, while for higher temperature models (the core of the spark channel along the axis of symmetry) the systems equilibrates very quickly, sometimes in less than 1 ns. To tie this back to our dog-rabbit analogy, this corresponds to an old, arthritic lap dog giving chase vs. a young, healthy, and hungry German Shepard!

From these results we now have an appreciation for how fast our systems can reach their equilibrium/stationary points. However, the question still remains of *how* they get there. We answer this question in the next section, Section III-D by examining a mathematical tool construct called the *Jacobian matrix*.

D. Dominant Interactions: Jacobian Matrix

In conservative dynamical systems, of which all time invariant Hamiltonians are, the phase space[§] Γ hypervolume is conserved [34]. However, only a small class of realistic differential systems are conservative; most are dissipative, or driven-dissipative dynamical systems[¶]. The basins of attraction of the two allowable fixed points in the differential systems we consider were calculated in Section III-B, and are itself (the unstable source), and all physically allowable space in Γ_C (the stable sink). This corresponds to a dissipative differential system [35]. If we were to sprinkle a cloud of initial conditions in this composition space Γ_C we would observe that their total volume V would decrease as a function of time. This volume would eventually collapse onto the stable sink like air being sucked out of shrink wrap surrounding clothes getting smaller and smaller. To prove this mathematically, we may write out how the evolution of a density of initial conditions $\rho(\vec{\eta}, t)$ changes as a function of time

$$\frac{d}{dt}\rho(\vec{\eta}, t) \equiv \frac{\partial \rho}{\partial t} + \sum_{\alpha=1}^{n_s} \frac{\partial \rho}{\partial \eta_\alpha}\frac{d\eta_\alpha}{dt}, \tag{15}$$

where we have expanded out by the chain rule the implicit dependence η_α dependence on time. Thusly, the evolution of the density ρ depends explicitly on the how the various species depend on time if we rearrange Eq. (15). In Hamiltonian

---

[‡] Numerical solutions to differential systems discretize both space and time. The minimum resolution is time here was 1 ns, hence the jumps/hops at 1,2,3,4, and 5 ns whose vertical distance is nonuniform in the Fig. 16.

[§] Within this document we have referred to two different spaces: composition space and phase space. Composition space refers to the space $\mathbb{R}_{+}^{+,n_s}$ within which the chemical kinetics species reside, while the total *phase space* refers to the total space the dynamics residing the total differential system where the electric field, electron temperature, and all other variable present in the differential system. The composition space has been referred to as Γ_C. The plasma phase space shall be Γ_P. The total phase space is $\Gamma \equiv \Gamma_C \oplus \Gamma_P$ where $\oplus$ is the vector space's direct sum.

[¶] The dissipative nature of these systems is closely tied to the second law of thermodynamics $dS \geq 0$ i.e. *global* entropy production

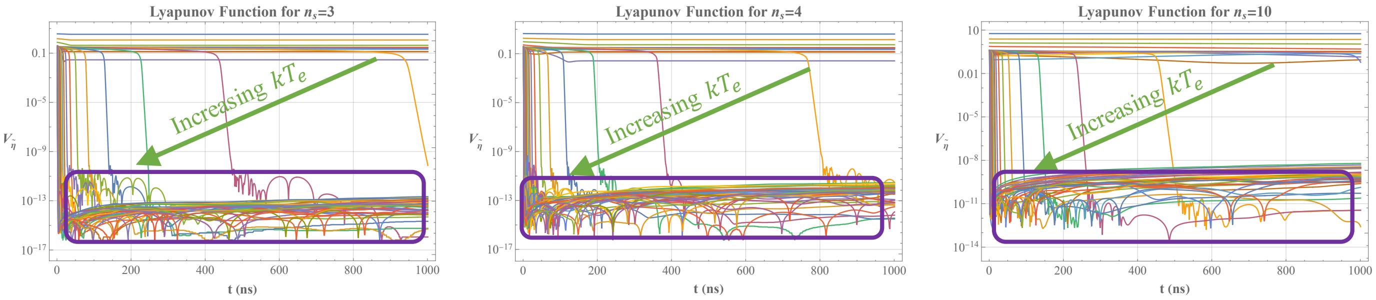

(a) $n_s = 3$ (b) $n_s = 4$ (c) $n_s = 10$

Fig. 15: Lyapunov function $V_{\widetilde{\eta}}(t)$ as a function of time.

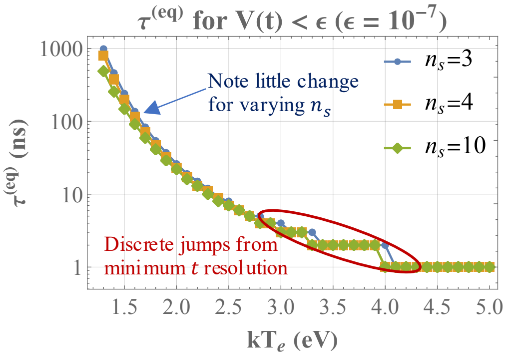

Fig. 16: Equilibration time for all Lyapunov functions as a function of temperature and n_s

systems it may be shown from Hamiltons equations [‖] that $\partial\rho/\partial t = 0$. In our analysis, however, $\partial\rho/\partial t$ equals $d\eta_a/dt$ with the assumption that volumes in Γ_C are $V_{\Gamma_C} \equiv \prod_{\alpha=1}^{n_s} \eta_\alpha$, which implies that ρ is linear in each η_α and that $\partial\rho/\partial\eta_\alpha = 1$.

We define the *Jacobian matrix* as

$$J_{\alpha\beta} \equiv \frac{\partial}{\partial\eta_\eta}\frac{d\eta_\alpha}{dt} \tag{16}$$

with α and β being indices ranging from 1 to n_s we may find the evolution volumes within this space as the trace of the matrix, $Tr(J_{\alpha\beta})$, in Eq. (16). Recall from general matrix theory that the trace of a matrix is the sum of its eigenvalues, and the determinant is their product. Due to conservation of species, the determinant of these matrices will always be zero (thusly $J_{\alpha\beta}$ is noninvertible/diagonalizable) while the trace is simply the sum along the main diagonal of the square matrix $J_{\alpha\beta}$.

In general, volumes in the composition space Γ_C will not evolve linearly due to the nonlinear nature of the equation presented within our nonlinear differential systems. Figure 17 shows a sample volume evolution in the $n_s = 3$ space spanned by η_1, η_2, and η_i. A cloud of initial conditions contained in $\mathbb{V}(0)$ will evolve under in time to the mutated volume $\mathbb{V}(t)$ whose structure will be given by the trace of Eq. (16). To aid in visualizing the differential systems interaction within the $n_s - 1$ dimension allowable space[**], we my construct matrix plots of the Jacobian matrix at different times. Figures 18 to 20 show sample images of the Jacobian matrix at the noted selected times. Each subfigure within these figures contains two different matrix plots that correspond to positive (green) and negative (blue) entries in the matrix. The color bar legend shows the base 10 exponent normalized relative to the maximum growth and decay rates occurring within the entire simulation. The darker colors are smaller growth(decay) while the brighter color are higher relative growth(decay). The simulations were run to 400 ns at a fixed electron temperature of 1.5 eV a representative calculation for expected channel dynamics/parameters.

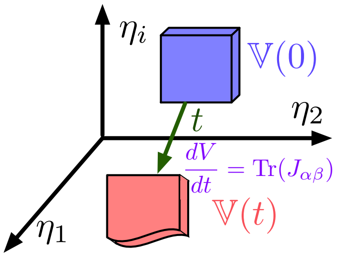

Fig. 17: Phase space volume evolution is determined by the trace of the Jacobian matrix, $Tr\,(J_{\alpha\beta})$. The shown phase space volume $\mathbb{V}$ corresponds to a cloud of initial conditions aggregated and evolved forward in time.

Figures 18 and 19 contain three separate matrix times slices that contain each of the relevant dynamical steps within the fixed temperature simulations, while Fig. 20 contains six different matrix time slices to understand simulations dynamic interactions. The color in the β column of the α row corresponds to how much species η_β is contributing(interacting) to species η_α's growth(decay).

The initial condition for growth(decay) is shown in Figs. 18a and 19a. As time progresses, the relative value of the growth

---

[‖] $d\vec{q}/dt = d\mathcal{H}/d\vec{p}$ and $d\vec{p}/dt = -d\mathcal{H}/d\vec{q}$ with $\vec{q}$ being the usual position coordinate, $\vec{p}$ being the usual momentum coordinate, $\mathcal{H}$ being the time invariant Hamiltonian, and t being time

[**] Recall that conservation of total species number will restrict the n_s dimensional composition space to a $n_s - 1$ hypersurface within that space. Flow in that space can only occur on that lower dimensional manifold. Mathematically this is because to one eigenvalue λ_γ of the Jacobian matrix $J_{\alpha\beta}$ is 0 due to conservation of total species number.

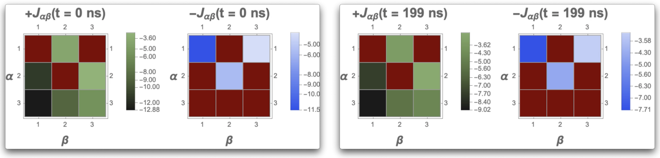

(a) $t = 0$ ns

(b) $t = 199$ ns

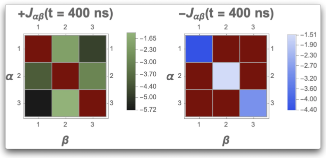

(c) $t = 400$ ns

Fig. 18: Jacobian matrix, $J_{\alpha\beta}$, movie snapshots with $n_s = 3$

changes as can be seen in Figs. 18b and 19b. At late time the simulation's dynamics and interaction completely change, and we can readily observe that all the diagonal elements are negative, correspond to volume "shrink wrapping" around the stable equilibrium. During the simulation interaction between different species change, see which cells in the matrix plots change from green to blue. In addition, we may be note that the brightest colors are the cells adjacent to the main diagonal forming an interaction ladder of nearest neighbors.

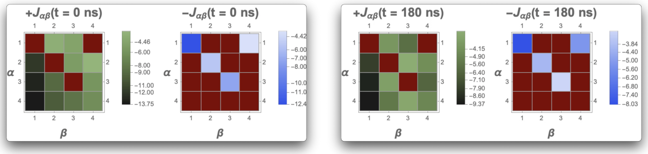

(a) $t = 0$ ns

(b) $t = 180$ ns

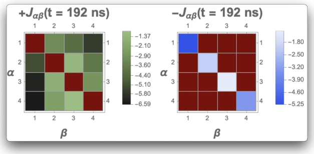

(c) $t = 192$ ns

Fig. 19: Jacobian matrix, $J_{\alpha\beta}$, movie snapshots with $n_s = 4$. The last shown time is $t = 192$ ns due to the simulation having reached equilibrium.

As we increase the dimensionality of our considered differential system for $n_s = 3, 4$ and 10, we may delve deeper into the relationships between variables. As before Fig. 20a shows the initial growth rate of each species correlating to all other species. As time marches forward in Figs. 20b to 20e, we observe that the decay of many species is associated with the ionized species η_i. As before, though, a common result through all time is that the dominant mode of interaction is by the interaction ladder of nearest neighbors, with each species wishing to become further excited is to step, one-by-one, up the ladder to the fully ionized state. In Fig. 20f we observe that as in Figs. 18c and 19c the negative entires all lie along the main diagonal, corresponding to "shrink wrapping" the stable sink.

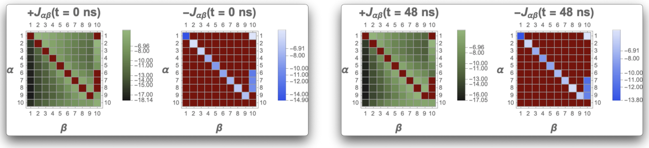

(a) $t = 0$ ns

(b) $t = 48$ ns

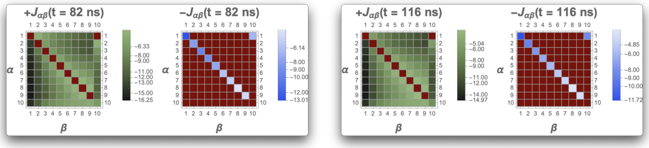

(c) $t = 82$ ns

(d) $t = 116$ ns

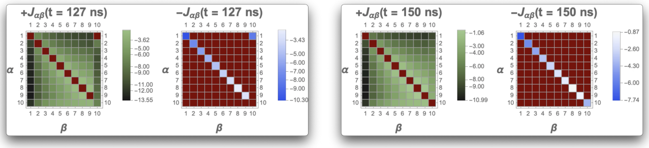

(e) $t = 127$ ns

(f) $t = 150$ ns

Fig. 20: Jacobian matrix, $J_{\alpha\beta}$, movie snapshots with $n_s = 10$. The last shown time is $t = 150$ ns due to the simulation having reached equilibrium.

The eigenvalues and eigenvectors of this matrix provide an alternative way inform us as to the critical interactions and timescales. Eigenvalues of a capacitive discharge system with $n_s = 3$ may be seen in Fig. 42 in Section V-E.

The differential system considered within this report can have arbitrary dimensionality depending on the accuracy one wishes to attain by modeling sample kinetic systems. However, there is a cost to this increasing dimensionality, greater computational expense. With higher dimensional (bigger n_s) systems, performing requisite analysis by calculating the dominant species, timescales, and interactions becomes more computationally burdensome. At some point we must ask ourselves the question as scientist and engineers with a final deliverable to meet: "What is "good enough" for our purposes?". One way to lower computational expense of this chemical kinetics analysis is to perform model reduction techniques from one of a multitude of perspectives: dynamical systems, statistical mechanics, and data science. Section IV goes into detail about the mathematical and preliminary results of finding the slow invariant manifold (SIM)[††]

IV. MODEL REDUCTION

Section III went into great detail delving into our considered n_s dimensional chemical kinetics differential system attempt-

---

[††] Other authors refer to this concept as the slow manifold. Here we shall use SIM to maintain consistency with cited literature.

ing to understand the dominant dynamics within in so that they could be leveraged in our ESD simulation toolset. We came to the conclusion in Section III-D that although highly detailed and accurate simulation are required from the microscopic perspective in the problem, the macroscopic energy budget balance behavior is mainly influenced by schemes that capture most of the relevant dynamics. Attempting to bridge these two needs of high fidelity for our role in creating a predictive toolset and also maintain computational tractability we have chosen to use reduction techniques to uncover the underlying, driving dynamics on the long timescale. These long timescale dynamics are mathematically a lower dimensional manifold, commonly referred to as a Slow Invariant Manifold (SIM) [36], [37], [38].

A. *The Intrinsic Low Dimensional Manifold*

In the field of combustion and flame kinetics mathematical techniques have been formulated to find objects in composition phase space Γ_C called the Slow Invariant Manifold (SIM). The SIM is a lower dimensional structure in composition space that draws all composition trajectories toward it on fast timescales, while trajectories along it advance slowly. The techniques were pioneered by Mass and Pope in 1992 [36] with application to coupled systems of nonlinear first order ODEs. These techniques gone through multiple different variations and refinements through the decades [39], [40]. Indeed, the idea of a slow manifold is not limited to the field of chemical kinetics [41].

The application of this technique pioneered by Maas and Pope is called the Intrinsic Low Dimensional Manifold. The basic idea of this technique is to project the fast dynamics (zapping like lightning) onto the slower dynamics (oozing like honey) of the kinetic differential system. As an illustration consider the following coupled, two dimensional, first-order, linear differential system

$$\dot{\vec{x}} = \underbrace{V\Lambda V^{-1}}_{A}\vec{x}$$

with $\dot{\vec{x}}$ being the first time derivate of $\vec{x} = (x_1, x_2)^T$. The matrix $V\Lambda V^{-1}$ is the diagonalized version of a constant coefficient matrix A. V is the matrix whose columns are the eigenvectors of A, and Λ is a diagonal matrix whose diagonal elements are the eigenvalues of A. Consider the differential system whose V matrix is $V = \begin{bmatrix} v_1 \, v_2 \end{bmatrix} = \begin{bmatrix} \frac{1}{\sqrt{2}} & \frac{1}{\sqrt{10}} \\ \frac{1}{\sqrt{2}} & \frac{3}{\sqrt{10}} \end{bmatrix}$ with the nonorthogonal eigenvectors $\vec{v}_1 = [\frac{1}{\sqrt{2}} \; \frac{1}{\sqrt{2}}]^T$ and $\vec{v}_2 = [\frac{1}{\sqrt{10}} \; \frac{3}{\sqrt{10}}]^T$. By varying the diagonal values of Λ (λ_1 and λ_2) we may observe disparate time scale behavior. Keeping $\lambda_1 \equiv \lambda_s$ a constant -1 we vary $\lambda_2 = \{-2, -5, -10\} \equiv \lambda_f$ for slow and fast eigenvalues, respectively. The results of varying this second eigenvalue associated with the eigenvector $\vec{v}_2$ is shown in Fig. 21. This figure contains the three different plots as $\lambda_2(\lambda_f)$ is varied. The 10 black dots correspond to percentage completion along the integrated time path from 0 to to t_end with four different initial conditions $\{\vec{x}^{(ic)}\} = \{(5,1), (2,5), (-4,-1), (-1,-4)\}$. The final time was set to 5 nondimensional time units. The blue and red text correspond the fast (zapping) and slow (oozing) eigenvalues and the associated eigenvectors denoting direction.

Figure 21a shows low disparate ratio λ_f/λ_s. Note for the four initial conditions how their linear solution behaves in this two dimensional space. The initial conditions along the higher value eigenvector zap into the stable equilibrium point of $\vec{x}^{(eq)} = (0,0)$, while the initial conditions with components in both $\vec{v}_1$ and $\vec{v}_2$ quickly zap out their projection along $\vec{v}_2$ to ooze/glide in along the slower eigenvalued eigenvector $\vec{v}_1$. As we increase the ratio λ_f/λ_s we see how these dynamics become more pronounced.

Our goal with the ILDM method is to uncover the lower dimensional motions along the slower direction like $\vec{v}_1$ and use that to reduce the dimensionality of the full differential system. For this simple, linear two dimensional model the dynamics are readily obtained by parameterizing the slow variable as the projection of the total dynamics onto the eigenvector $\vec{v}_1$. However, for higher dimensional examples, see Fig. 22, that have nonlinearity and *changing* eigenvalues as a function of location in phase space these dynamics are more complicated and a more rigorous method is required in order to determine the SIM/ILDM.

In the dynamics that we observe in our constructed differential system we observe three distinct species clusters present within the simulations, Fig. 23, implying that the minimum dimensionality of the system is three: $n_{s,min} \approx 3$. To determine if this is true we have plotted parametric pairwise plots of the variables η_α vs η_β in Figs. 24 to 26. These plots were at fixed electron temperature of 1.5 eV and were run from $t_0 = 0$ to $t_{end} = 400$ ns. The colorbar at the right of every plots shows the implicit, parametric variable time, t. The horizontal and vertical axes are the nondimensional base 10 exponent of the species $\widetilde{\eta_\alpha} = \eta_\alpha/\eta_0$ where η_0 is the total of all species populations (a conserved quantity).

The constructed $n_s \times n_s$ matrix plots showing $(\eta\alpha(t), \eta_\beta(t)) : t \in (0, t_{end})$ have several interesting observables:

- Only the upper(lower) diagonal parts of the matrix plots are useful, as the plots are mirrored from on the opposite side of the diagonal.
- The equilibrium solution is always reached fairly early on, especially as the dimensionality n_s of the system increases.
- Most of the relationships between the species are linear. See the lower middle section of Fig. 26 for this.
- Many of the dynamics zap quickly and then ooze along to the equilibrium solution $\vec{\eta}^{(eq)}$.

From these observations and the fact that we heuristically suspect that a three dimensional system is all that is necessary to capture the relevant dynamics of these vibrational models

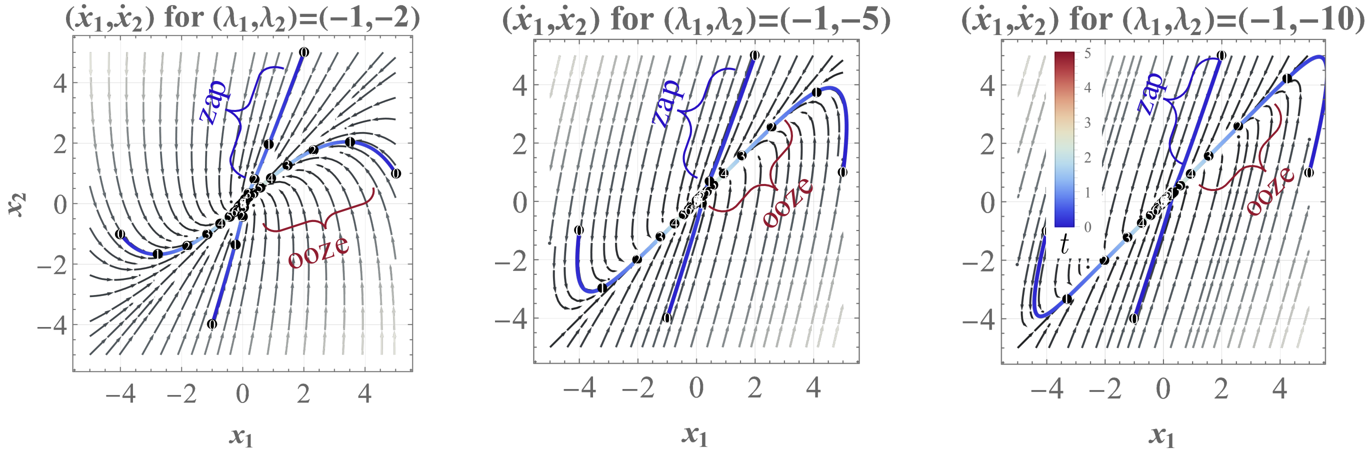

(a) $\lambda_2/\lambda_1 = 2$

(b) $\lambda_2/\lambda_1 = 5$

(c) $\lambda_2/\lambda_1 = 10$

Fig. 21: Progressively disparate ratio of λ_s/λ_f, with $\lambda_s \equiv \lambda_1$ and $\lambda_f \equiv \lambda_2$. The numbered black dots correspond to the i'th times 10 percent completion along the trajectory, $\vec{x}(t)$ where $t \in (0, t_{end})$ with $t_{end} = 5$. The time colorbar is embedded within Fig. 21c. The grey arrows show the local direction of the flow in this two dimensional phase space Γ. The blue to red colored lines are the trajectories of four different initial conditions $\{\vec{x}^{(ic)}\}$

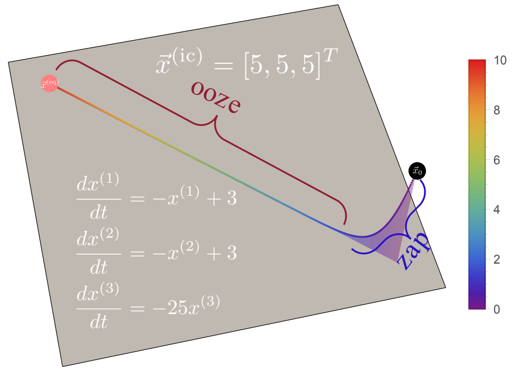

Fig. 22: Three dimensional zap-ooze manifold schematic.

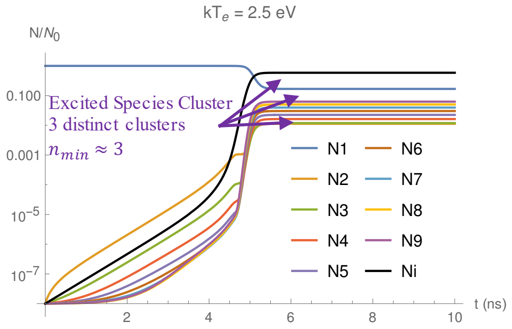

Fig. 23: Sample chemical kinetics simulation clustering into three distinct species.

we chose the lower left plot in Fig. 24 as the manifold to uncover with Maas and Pope's technique. As described in the paper by Maas and Pope, we may use conservation of species to further reduce the dimensionality of the model from $n_s = 3$ to $n_s - 1 = 2$. Furthermore, by the judicious choice of a single valued function to parameterize, we choose the parameterized reaction coordinate as η_i. This simplifies our analysis considerably from a n_s dimensional problem to a 1D numerical root finding problem.

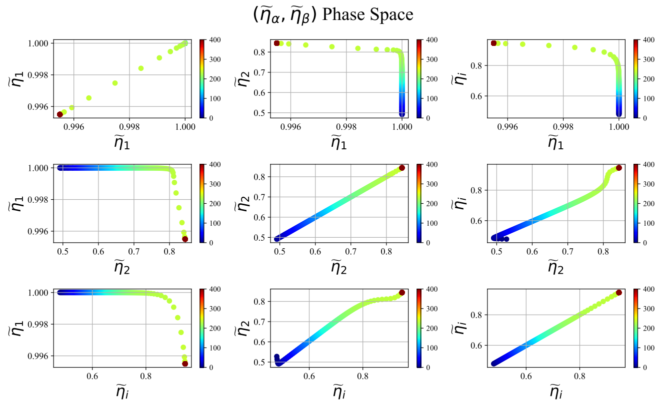

Fig. 24: $n_3 \times n_3$ matrix of parametric phase space plots for a 3 level kinetic system: ground, one excited, and ions.

The equations used in the ILDM analysis are reproduced here for the reader's convenience and interest. Beginning with the evolution equations for the species in the base 10 change of variables space we have

$$\frac{d}{dt}\eta_\alpha = f_\alpha(\vec{\eta}) \approx \eta_{\alpha,0} + \underbrace{\frac{\partial}{\partial \eta_\beta} f_\alpha(\vec{\eta})\,(\eta_\alpha - \eta_{\alpha,0})}_{\text{Jacobian matrix } J_{\alpha\beta}} + \underbrace{\mathcal{O}\left((\eta_\alpha - \eta_{\alpha,0})^2\right)}_{\text{ILDM error}} \tag{17}$$

with $\eta_{\alpha,0}$ being the value that is being expanded about, the SIM, the second term on the right hand side is similar to the Jacobian matrix $J_{\alpha\beta}$ from our previous analysis in Section III-D, and the third term on the right hand being error of order $(\eta_\alpha - \eta_{\alpha,0})$ which we discard if we are close the point

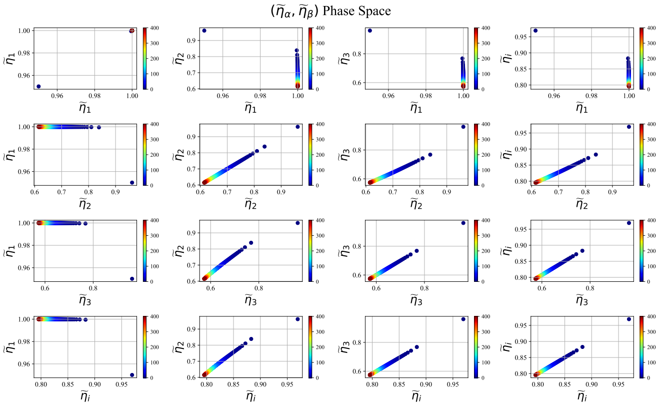

Fig. 25: $n_4 \times n_4$ matrix of parametric phase space plots for a 4 level kinetic system: ground, two excited, and ions.

we are expanding about $\eta_{\alpha,0}$ (the SIM). The Jacobian matrix analogue may be diagonalized, Eq. (18). This diagonalized Jacobian may be substituted into Eq. (17).

$$\frac{\partial}{\partial \eta_\beta} f_\alpha(\vec{\eta}) = V \Lambda V^{-1} = \begin{bmatrix} V_f V_s \end{bmatrix} \begin{bmatrix} \Lambda_f & 0 \\ 0 & \Lambda_s \end{bmatrix} \begin{bmatrix} V_f^{-1} \\ V_s^{-1} \end{bmatrix} . \qquad (18)$$

The Jacobian matrix is separated into the fast (zap) and slow (ooze) timescales. $V_f(V_s)$ is the matrix whose columns are the eigenvectors of the fast(slow) part of the Jacobain matrix, see Fig. 27[‡‡]. $\Lambda_f(\Lambda_s)$ is the diagonal matrix of the fas(slow) eigenvalues. There are $l_f(l_s)$ fast(slow) eigenvalues. The dimensionality of the system is $n_s = l_f + l_s$. After substituting Eq. (18) into Eq. (17) and multiplying by the inverse eigenvector matrix $\begin{bmatrix} V_f^{-1} \\ V_s^{-1} \end{bmatrix}$ and using the product rule we then have

$$\frac{d}{dt}\phi_\alpha = \underbrace{V^{-1}\eta_{\alpha,0}}_{①} + \underbrace{\Lambda\phi_\alpha}_{②} + \underbrace{\Delta\eta_\alpha \frac{d}{dt} V^{-1}}_{③} \qquad (19)$$

with ϕ_α being the eigenvector coordinates which are orthogonal(transverse) to the SIM for fast(slow) dynamcis, and $\Delta\eta_\alpha = \eta_\alpha - \eta_{\alpha,0}$. ① is the term that we solve for along the SIM, ② is the term that is defined to be 0 on the SIM (the zapped out motions in the phase(composition) space $\Gamma(\Gamma_C)$), and ③ is assumed to be approximately zero on the manifold (the change in the orientation of the fast eigenvectors is assumed to occur on a scale that is much slower than the SIM dynamics; the SIM is assumed to have little curvature.). Finally, we arrive at the equation that we wish to solve numerically in order to obtain our SIM

$$\Rightarrow V_f^{-1}\eta_{\alpha,0} = 0 \text{ for } \textit{ILDM} . \qquad (20)$$

Solving Eq. (20) numerically for the lower left plot shown in Fig. 24 we obtain the blue points in Fig. 28. The text on the figure annotates various items that were accomplished. Note that there were numerical challenges associated with certain region on the calculated SIM. The green line, a 1D manifold, is the interpolated SIM, and would be the structure that would be used to project our $n_s - 1 = 2$ dynamics onto.

As with any numerical method there are some drawbacks and caveats to applying the ILDM technique. Applying this technique makes several assumptions, see the reproduced mathematical derivation above, about the dynamics inherent within the system. Another very important assumptions that is made when doing this analysis is that the eigenvectors do not change direction too rapidly, and that their associated eigenvalues maintain their relative ordering in Eq. (18) and Fig. 27 [38]. If either of these assumptions or caveats are breached, then this method is no longer applicable. This has not occurred in the any of the differential systems that have been considered within this report, but it is a consideration to take into account when applying this dynamical system approach to dimensionality reduction.

To gird ourselves against the potential of this occurring we may broaden our dimension reduction options and explore other possible alternatives. Two other methods have been briefly explored and a preliminary literature review has been undertaken to review these two other methods: Boltzmann grouping which is motivated by the clustering of distinct vibration states within our chemical kinetics differential system, recall Fig. 23; and a data driven approach called Principal Component Analysis (PCA). A description of these methodologies is given in the next section, Section IV-B

B. Alternative Reduction Methods: Principal Component Analysis & Boltzmann Grouping

In Section IV-A we showcased a dynamical systems approach to reducing the dimensionality of our constructed chemical kinetics differential system. That approach uncovered the underlying slow manifold that is postulated to be inherent within systems of disparate timescales as evidenced by performed numerical simulation. The fast timescale eigenvectors are orthogonal to the manifold; in order to numerically obtain this structure, we set the directions of those fast motions to zero to obtain the lower dimensional slow manifold parameterized by the slow eigenvectors, Eqs. (17), (19) and (20) (n_s dimensional manifold with $l_f + l_s$ fast and slow directions, respectively). This approach netted us the interpolated green curve in Fig. 28.

This section describes two other approaches that are motivated by observations of more detailed chemical kinetics systems (a statistical physics method), and a data driven approach motivated by the large amounts of data generated by these high dimensional rate equations.

Our statistical physics approach, called Boltzmann grouping, is motivated by the distinct clustering of species in certain sim-

---

[‡‡] Since the eigenvalues of the linearized coefficient matrix of system of ODEs correspond to inverse time, $1/t$, the larger the eigenvalue is the slower (more oozy) the motion along that characteristic direction will be.

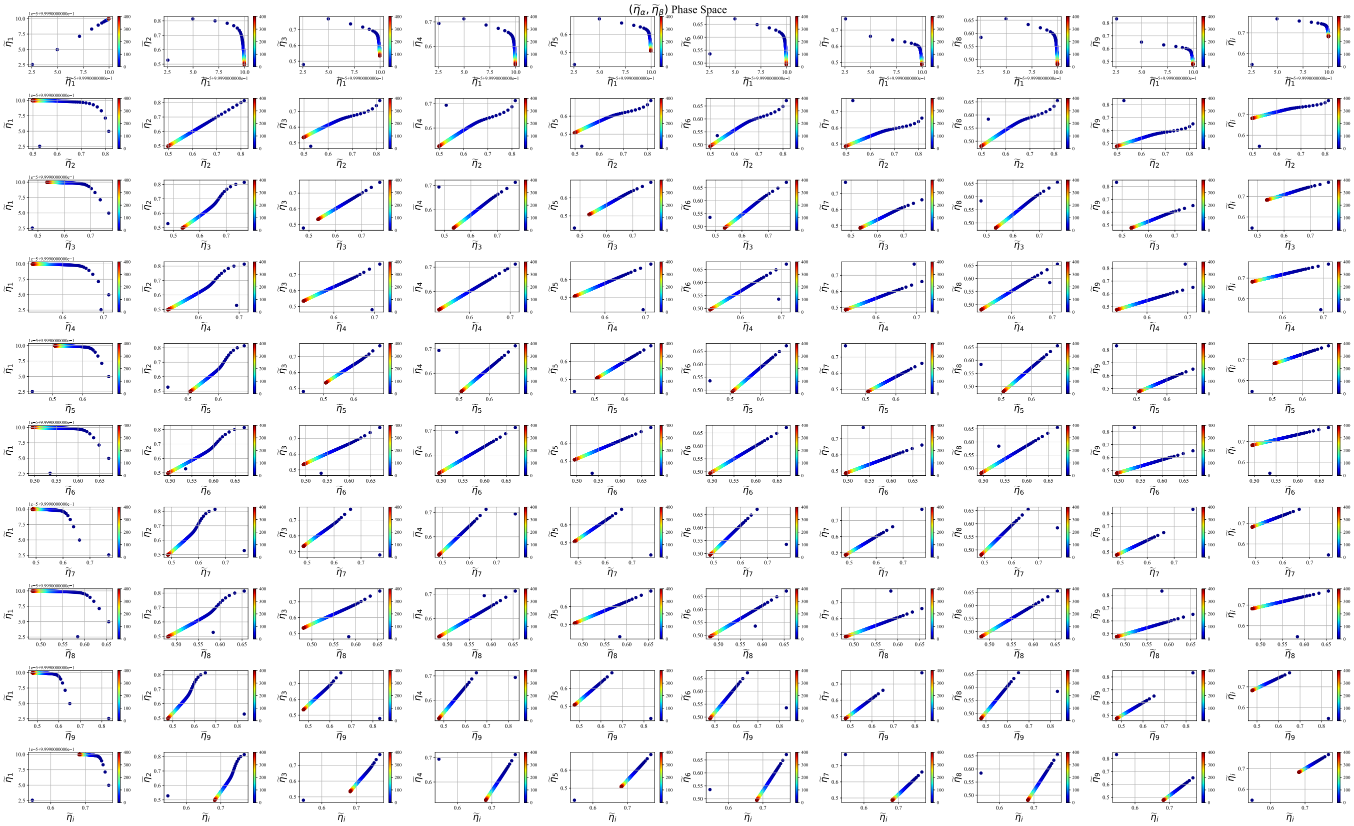

Fig. 26: $n_{10} \times n_{10}$ matrix of parametric phase space plots for a 10 level kinetic system: ground, eight excited, and ions.

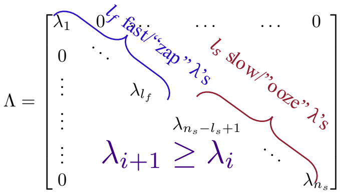

Fig. 27: Diagonalized Λ matrix showing the separation between slow and fast modes of the differential system.

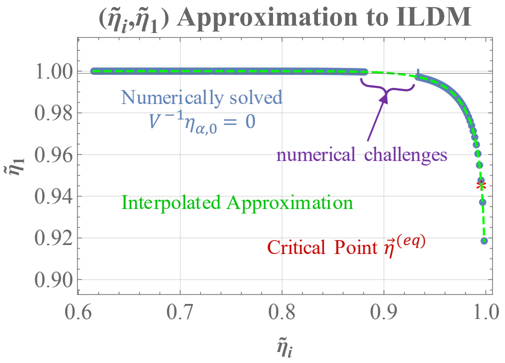

Fig. 28: Obtained 1D slow invariant manifold for our reduced 2 level system. Proof of concept.

ulations, see Fig. 29. This figure has several distinct, colored species groups that all qualitatively evolve together. Boltzmann grouping seeks to leverage this fact and cluster these distinct vibrational species together [42], [43]. In equilibrium the populations of various species levels will be determined by their relative energy differences $\Delta E_{\alpha\beta}$ between vibrational levels α and β. The methodology detailed in [42], [43] details how to leverage this fact and reformulate the differential system to reduce its dimensionality.

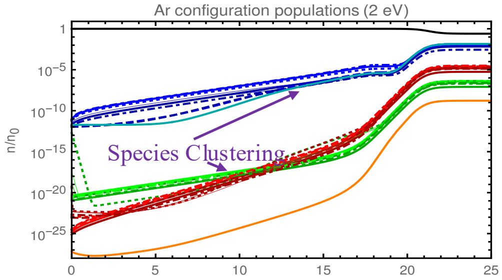

Fig. 29: Groups of species clustering into distinct groups. Reducing methods may be leveraged to establish more tractable models.

Another method that may be used to reduce the dimensionality of a differential system is to project the 0D dynamics of the chemical kinetics differential system onto the most informative/important finite, low number linear combinations of all the original chemical kinetics variables. This is called Principal Component Analysis (PCA) of the coupled, chemical kinetics differential system [44], [45].

This is accomplished by:

1) Measuring a matrix, $\mathbf{X}_0$, whose dimensions are $[n_{data} \times n_s]$ with n_s being the usual number of chemical kinetic species and n_{data} being the number of discrete time points that are being measured. The usual time integration steps are assumed for this PCA method to work properly.
2) Scaling this data matrix by subtracting the averages of every measured column variable and also by multiplying by one over the standard deviation of the distribution, normalizing the data: $X = \left(\mathbf{X}_0 - \bar{\mathbf{X}}_0\right)\mathbf{S}$. The matrix $\mathbf{S}$ is the matrix of the inverse standard deviations of the column variables of $\mathbf{X}$ and $\bar{\mathbf{X}}_0$ is the matrix of the averages of $\mathbf{X}_0$.
3) Obtaining a correlation matrix $\mathbf{C}_X = \frac{1}{n_{data}-1}\mathbf{X}^T\mathbf{X}$ which measures the correlations of the species with each other throughout the entire simulation. The correlation matrix may be diagonalized in the usual way $\mathbf{C}_X = C_X = V\Lambda V^{-1}$ with the matrix $\mathbf{V}$ being the matrix whose columns are the eigenvector of $\mathbf{C}_X$. Most of the correlation matrices' variance is recorded in the first few $q < n_s$ variables.
4) The PCA variables, which are the largest eigenvectors of $\mathbf{C}_X$ may be calculated by $\mathbf{X} \approx \mathbf{X}_q = \mathbf{Z}_q\mathbf{V}^{-1}$.

The truncated matrix $\mathbf{X}_q$ has dimension $[n_{data} \times q]$. It may be inserted into the chemical kinetics differential system which can be reformulated into an appropriate form [44], [45].

Boltzmann grouping (statistical mechanics) and PCA (data driven) are just two alternatively motivated methodologies that may be used in order to reduce the dimensionality of the chemical kinetics system. These techniques may be used to make the chemical kinetics system more tractable both for analytical and computational treatment. We seek to utilize these techniques to evolve our ESD simulation toolset, which to date in its most useful form has solely implemented a "blind" heat source that has taken data both from COMSOL multiphysics chemical kinetics [12] and also from legacy and current experimental current traces [13]. The details of the work taking motivation from legacy and current experimental data is detailed in Section V.

V. HYDRODYNAMIC SIMULATION

Quantifying the energy budget in ESD events is one of the main objectives of the ESD Weapon Response Initiative. There are many ways for energy to flow within the interwoven, constituent physics present within ESD events, Fig. 3. We seek by architecting a ESD simulation toolset to attack many of the problems inherent within Weapon Response frameworks with a (not overly) conservative, physics-based basis. One of the legs of this basis is the hydrodynamics which we know dominates the physics far away from the channel. What we don't fully know is how much impact early time hydrodynamic flow advection of thermodynamic variables affects the characteristic plasma variables of ESD events (spark resistance R_s, energy/power delivered to victim load E_v/P_v, etc.).

Within this section of the report, we detail how we have established conservative bounds on the energy going into the hydrodynamics and shockwave formation/propagation that is *guaranteed* to be unavailable to plasma variables of interest. We do this by: motivating the performed simulations by legacy and current experimental data; comparing to decades of available literature; and theoretically verifying against the strong, intermediate, and weak shock regimes. Finally, we enumerate the computational intricacy, challenges, and propose a future path forward of combining the explicit hydrodynamic based solver whose fastest dynamics are shockwaves (μs/ms) to the comparatively fast (ps/ns) timescale dynamics of the chemical kinetics interactions Section III-D.

A. Empirical Heat Source Motivation

In prior work performed by W-10's R&D arm we looked at two ways to implement a blind heat source in to a well developed, mature hydrodynamic code called Fierro [21], [22]. The first work examined inserting a heat source calculated directly from an early time evolution of the COMSOL Multiphysics commercial software for chemical kinetics and hydrodynamic flow absent shockwaves. The work resulted in the early time verification of Fierro for use in ESD spark events. The second arm of the research involved postulating a heat source substantiated by decades of literature and legacy/current LANL experiments.

The temporal nature of the heat source is assumed to come from the Joule Heating term of magnetohydrodynamcis $\vec{J}\cdot\vec{E} = \vec{J}^2/\sigma$ where $\vec{J}$ is the area current density, $\vec{E}$ is the axial electric field in the channel, and σ is the conductivity of the medium. Legacy (Fig. 30a) and current (Fig. 30b) experiments performed at LANL, see Fig. 30, have two common features: a fast rise time on the order to tens of nanoseconds, and a decaying exponential envelope. These two features have informed our choice of $q(t) \equiv \left(1 - e^{-t/\tau_r}\right)e^{-t/\tau_f}$.

We assume the spatial nature of the heat source to be Gaussian, as substantiated by decades of available literature estimating the spatial structure of the ESD's channel [46], [47], [48].

Combining these two terms we then have both $q(r)$ and $q(t)$ which form the basis of the structure for $q(r,t)$. However, we still have a free parameter for the strength of these terms for the Joule Heating source (a power density) q_0. Based on conservation of energy (more specifically energy line density E_0/h) over the requisite time and spatial scales we may obtain an expression for q_0, see Eq. (22). A sample plot of $q(r,t)$ may be seen in Fig. 32.

$$q(r,t) = q_0\, \overbrace{e^{-r^2/\lambda_R}}^{q(r)} \overbrace{\left(1 - e^{-t/\tau_r}\right)e^{-t/\tau_f}}^{q(t)} \tag{21}$$

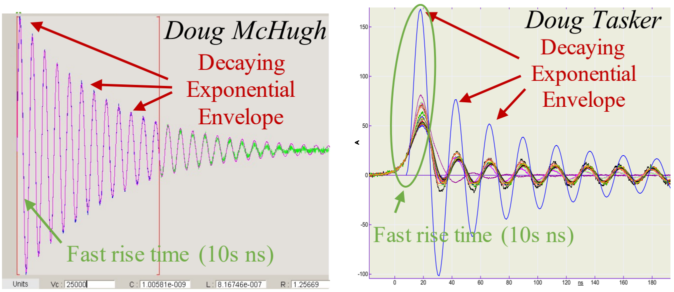

(a) Doug McHugh's and Michael Murphy's legacy current data.

(b) Doug Tasker's modern current data.

Fig. 30: Legacy and modern current traces taken by Doug McHugh (Q-6, LANL) Michael Murphy (Q-6, LANL), Doug Tasker (Q-6, LANL), and their respective teams. Note the fast rise time on the order of tens of nanoseconds and the decaying exponential envelope on the order of hundreds of nanoseconds. These experiments correspond to inductive discharges (longer timescale); our current models are capacitive (short timescale)

$$q_0\left(\frac{E_0}{h}, \lambda_R, \tau_r, \tau_f\right) = \frac{\tau_r + \tau_f}{\pi {\lambda_R}^2 {\tau_f}^2} \frac{E_0}{h} \tag{22}$$

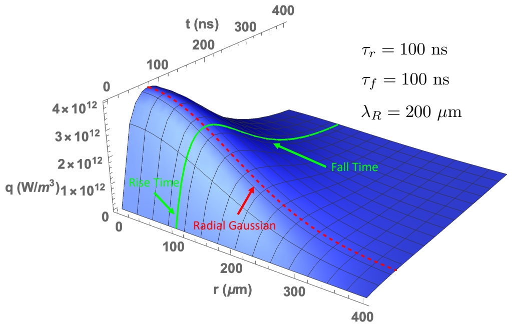

Fig. 31: Plotted heat source q_0 with given, fixed parameters λ_R, τ_r, τ_f and with a fixed value for E_0/h.

The four terms E_0/h, λ_R, τ_r, and τ_f form a four dimensional parameter space that may be searched and scanned to match legacy optical experimental images of ESD events. The simulation that minimize the metric of shockwave distance obtained from the legacy optical experimental images of the ESD events will then be validated. The details of how this is done are discussed in Section V-B.

B. Hydrodynamic Simulation Validation

A key part of the laboratory's mission is stockpile stewardship. This stewardship is underwritten with the marriage of experiment, simulation, and theory. In the past decades, simulation has come to a forefront. However, we are required to validate (compare to experiment) and verify (compare to theory) these simulation's results to ensure they have high fidelity/credibility necessitated by the work that we at LANL perform as given in our mandate.

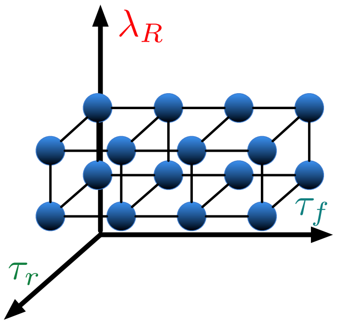

Fig. 32: Sample parameter space $(\tau_r, \tau_f, \lambda_R)$ for the hydrodynamic suite of simulations for fixed E_0/h.

To validate the simulations described in Section V-A we compared to legacy optical imaging data of the direct spatiotemporal evolution of the shocks created by the ESD event. This data was taken by Michael Murphy, Doug McHugh, and their collaborators in the late 2000s. This data has been used to validate our simulation suite. A schematic of the experimental setup may be seen in Fig. 33 [49], [50], with direct optical data taken by the framing camera shown in Fig. 34.

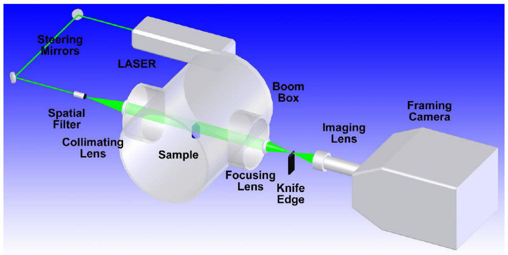

Fig. 33: Cartoon for the the Shock Wave Image Framing Technique (SWIFT) experiment. Laser light is shone and captures high-fidelity optical images for use in simulation validation to experiment.

Figures 34a to 34c show the spatiotemporal evolution of the shock wave away from the axis of symmetry in an ESD experiment. These images were chosen from an available suite of data due to their proximity to idealized cylindrical structure which aided our parameter space validation. Non-ideal structures, divergence away from cylindrical geometry, and "fingering" out (as common Lichtenberg figure) phenomena in lightning all contribute to the breakdown from our simplified $x - y$ plane quadrant, axially symmetric model.

Lin (1954) introduced a strong shock solution in cylindrical geometry [51] starting from an infinitely concentrated line source using a similarity solution. In his solution method he postulated that the radius of the shockfront as a function of time was $r(t) = S(\gamma)(E/\rho_0)^{1/4}t^{1/2}$ with $S(\gamma)$ being a tabulated value dependent on material properties with units of length, E being the energy line density deposited into the medium, ρ_0 being the ambient density, and t being time. For air $S(\gamma) \approx 1.009$ and $\rho_0 = 1.00$ at Los Alamos's altitude. Postulating a fit for the evolution of the shock radius $r(t) = 1.009 \times a \times t^b$ we fitted to both experimental from

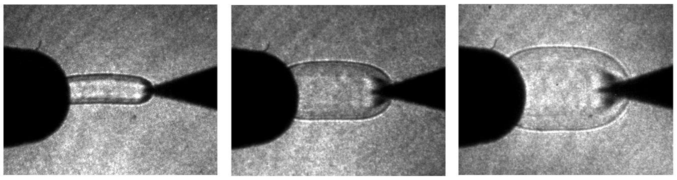

(a) $t - t_{soc} \approx$300ns (b) $t - t_{soc} \approx$2.0μs (c) $t - t_{soc} \approx$3.6μs

Fig. 34: SWIFT high speed direct optical images detailing spatiotemporal evolution of an ESD spark event. The gap between the two electrodes was 6.28 mm while the charging voltage was 15 kV. The caption below each figure denotes the time, t, from the start of current, t_{soc}, that triggers data collection.

Michael Murphy's legacy experiment and simulation data shown within this report.

Table I shows results of fitting equations for experimental results (exp) and simulation (sim). The value of both types of fit's exponents b very close to the theoretical exponent of $1/2$. The fitted a value roughly corresponds to the energy line density in the discharge event. These a values may be used in order to quantitatively determine the energy *guaranteed* to be going into the hydrodynamics.

TABLE I: f

Shot #	t_{soc} (ns)	a_{exp}	b_{exp}	a_{sim}	b_{sim}
1	-26 to -14	1.54 - 1.58	0.57 - 0.59	1.59	0.56
2	-16 to -8	1.83 - 1.89	0.55 - 0.57	1.89	0.55
3	-12 to 4	1.96 - 2.04	0.54 - 0.57	2.02	0.54
4	-20 to -8	2.00 - 2.06	0.54 - 0.57	2.05	0.54

The shock radius may be determined directly from the high-speed optical imaging data shown in Figs. 34a to 34c. We took four different experimental datasets with images of the shock propagating. Figure 35 shows the location of all four different experiments with the comparison to Lin's fit with the values excised from Table I.

We may validate our simulations by comparing the best fitting solutions from our available parameter space and compare that directly to the calculated shock front locations shown in Fig. 35. Figure 36 shows this comparison directly with the input energy parameter q_0 calculated from the experiments radial a parameters. One major thing to note is that with these comparisons the best results were returned with simulations that had short fall times, which correspond to a capacitive discharge. Further on in our work we implement a trial capacitative discharge that couples our hydrodynamics code which are described in detail in this sections and the chemical kinetics differential system discussed in Section III and a circuit coupled ODE. This process is discussed in Section V-E.

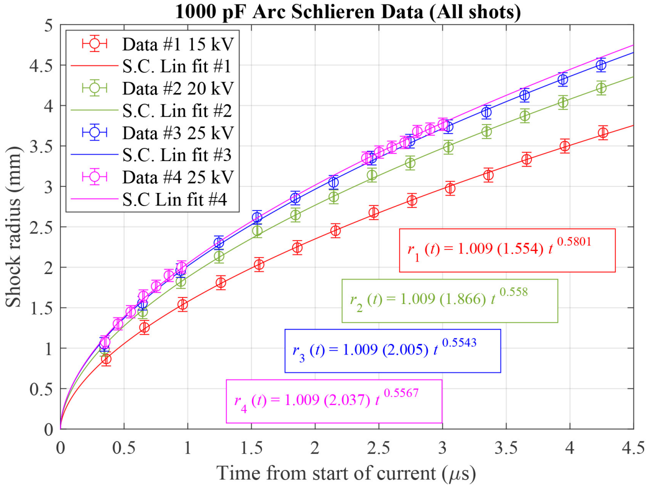

Fig. 35: Shock radii captured from high-speed optical data, see Fig. 34. Four different characteristic experiments were chosen that exemplify shock dynamics across a range of voltages.

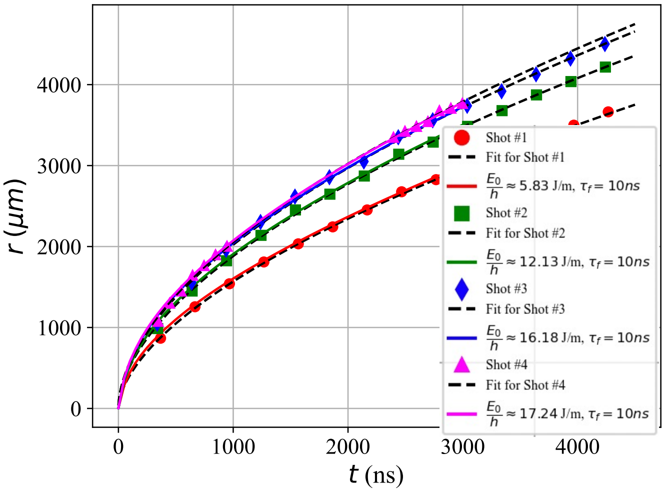

Fig. 36: Fitted shock radii excised from Fig. 35 and compared to optimized characteristic heat source parameters with the specified E_0/h, $\tau_r = 10$ns, $\tau_f = 10$ns, and $\lambda_R = 100\mu$m

C. Hydrodynamic Simulation Verification: Comparison to Shock Regime Theory

The last leg of the stool in Fig. 2 we have yet to explicitly discuss in the context of ESD events and their constituent hydrodynamics is theory. There has been much done and worked on in shock theory [52], [31], [53], [54]. We shall discuss cylindrical shock theory, explicitly: Lin's strong shock similarity solution [51], weak shock theory [52], and intermediate shock theory [55].

The reduced differential system that Lin solved for the shock structure behind the strong shock's shockfront is reproduced for convenience here in Eqs. (23a) to (23c).

$$f' = \frac{2\eta\left(\eta-\phi\right)+\gamma\phi^2}{f-\left(\eta-\phi\right)^2\psi}\frac{\psi f}{\eta} \tag{23a}$$

$$\phi' = \frac{f'-\gamma\psi\phi}{\gamma\psi\left(\eta-\phi\right)} \tag{23b}$$

$$\psi' = \frac{\left(\eta\phi'+\phi\right)\psi}{\left(\eta-\phi\right)\eta} \tag{23c}$$

The terms in the above equations: f correspond to pressure p multiplied by the radius of the cylindrical shockwave squared R_s^2 so $f \equiv p/p_0 R_s^2$ where p_0 is ambient pressure; ϕ corresponds to radial flow velocity u_r multiplied by the radius so $\phi \equiv u_r R_s$; ψ is the nondimensionalized mass density ρ so $\psi \equiv \rho/\rho_0$ where ρ_0 is ambient density; and η is the normalized radius ($\eta \in (0,1)$) of the characteristic flow variables. Figure 37 shows the numerical solution (correspondingly colored) to this coupled differential system for f, ϕ, and ψ as functions of η.

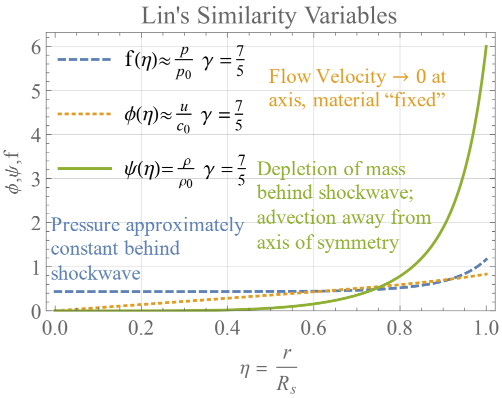

Fig. 37: Lin's similarity solution to a strong shock in cylindrical geometry arising from an infinitely concentrated line source of line energy density, E_0/h. The horizontal axis is $\eta \equiv r/R_s$ where R_s is the radial location of the shock front.

To verify our numerical simulations to cylindrical strong shock theory we may excise the normalized density profile $\psi(\eta)$ from Fig. 37 and compare that or density slices between the axis of symmetry and the shock radius R_s in our simulations. Figure 38 shows a 3D plot of the normalized density in our simulation suite taken at various time radial points. The maximum density shown in the plot is ≈ 6 as predicted by the Rankine-Hugoniot jump conditions $\rho_s/\rho_0 = \left(\gamma+1\right)/\left(\gamma-1\right)$ (this is also shown in Fig. 37). Note how the shockfront propagation in the (r,t) domain is nonlinear, with the density "quickly" decreasing from it's predicted maximum.

To compare to the semi-analytic solution that Lin predicted we may excise from Fig. 38 density profile at various times. This is then compared to the green density profile in Fig. 37. The result is Fig. 39 which shows the excised green density profile as a thick black line, and the various colored markers our simulation's results. Note at early times good agreement between simulation and theory while for later times the simulation diverges away from the theoretical strong shock solution. A major discrepancy between theory and the simulations is highlighted in the plot with the purple text noting the nondimensional location of a "kink" in the density line profile. This "kink" is due to the finite region where the shock forms in reality and the simulation, whereas the theory comes from an infinitely concentrated axial line source. The kind has be referred to, and we interpret it as, the material interface, contact discontinuity, or shell in the fluid medium.

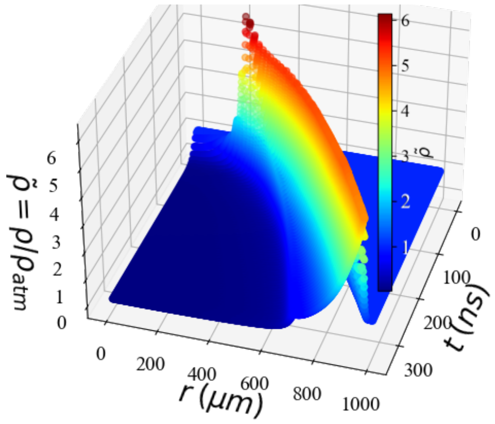

Fig. 38: Mass density, ρ, plotted as a function of space, r, and time, t. The highest amount for the normalized mass density is 6, as determined by strong shock theory [31], [52].

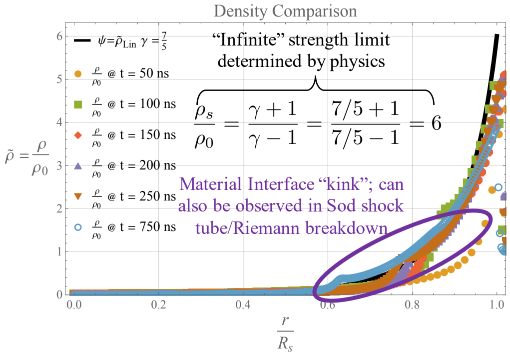

Fig. 39: Lin's similarity solution to the mass density plotted as a function of the normalized radial coordinate r/R_s. Plotted in comparison to this theoretical mass density are the mass density from our experimentally validated simulations captured at the noted times. At early times we have good agreement to the strong shock theory, but at later times divergence due to irreversibilities (artificial viscosity), and shock regime transition deviate the computational solution from Lin's solution.

Now that we have validated our empirically motivated simulations to experiments and verified to strong shock limiting theory we may delve and detail the structure of thermophysical variables. We have chosen the thermophysical variable mass density ρ for this purpose because mass density is the most informative variable due to conservation equation structure[§§].

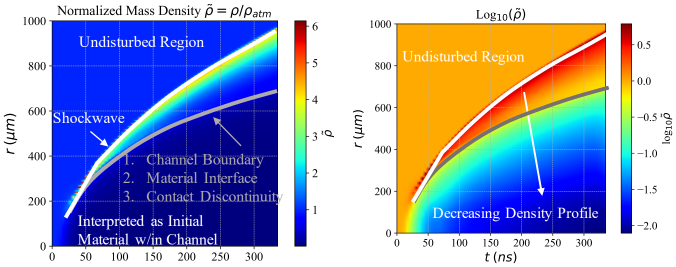

(a) Linear plot of the mass density, ρ, plotted as a function of space, r, and time, t.

(b) Log_{10} plot of the mass density, ρ, plotted as a function of space, r, and time, t.

Fig. 40: These plots are a projection onto 2D of Fig. 38. Note the grey and white lines which trace the channel discontinuity and shockwave, respectively. The continued difference in the density behind the channel boundary shows that continued advection is occurring, ensuring hydrodynamics as an energy terminus.

The 3D density plot shown in Fig. 38 may be more readily analyzed in a 2D map projection, see Fig. 40. Figure 40a shows a linear 2D projection. Here we may readily observe the white line as the shcokwave propagating radially as a function of time, whereas the gray line corresponds to the material interface/contact discontinuity, and is the “kink” as seen in Fig. 39. The “kink” also propagates out radially from the deposition of energy within the core of the channel. We may be note that the propagation speed, the slope, of the lines in the plot are both falling off. This behavior will eventually asymptote to the shockwave decaying to a weak shockwave and then asymptoting to an acoustic wave, while the contact discontinuity will stop moving as seen in some of our prior work [2], [3], [4], [13].

The usual characteristic scales of shock wave are km/s or mm/μs. This characteristic scale for shockwaves is further reduced for ESD events to the micron and nanosecond scale due to geometrical considerations. Reflecting this characteristic scale, our simulation’s shockwave dynamics is indeed on the order of hundreds of microns and tens of nanoseconds (which is also a reflection of the empirical heat source we have posited). Approximately 20 nanoseconds after the “initiation”[¶¶], we may see a shock forming, but it hasn’t fully formed yet to due not enough energy being deposited during the discharge yet. At 30 nanoseconds, we see the strong shock having formed in Fig. 38, due to the maximum density $\widetilde{\rho} = 6$ being reached. This shock is being driven by the gradient in pressure behind it and an effective piston which is the channel boundary. Eventually the shockwave separates from the piston[***] at approximately 75 nanoseconds, see Fig. 40a. Now we observe three distinct regimes of flow in the simulation domain, recall Fig. 9.

A natural question to ask when observing these regimes of flow is what is the general variation in these regions? The quiescent medium is non-varying, while the regions between the shockwave to the contact discontinuity and the contact discontinuity to the axis of symmetry vary but with marked difference. To more readily grasp the large differences in flow we may take a $\log_{10}$ transformation of the normalized density variable $\widetilde{\rho}$, see Fig. 40b. The biggest takeaway from this plot is the continued stratification in $\rho(r)$ caused by hydrodynamic advection away from the axis of symmetry. This advection ensures that the hydrodynamic mode is indeed an energy sink from the perspective of the victim load.

In addition to looking at the density we to compare to the explicit strong shock limit behind the shockwave radially we may look at the strength of the shockwave as determined the the overpressure. Overpressure is defined as a normalized difference in the pressure from ambient $\Delta p \equiv (p - p_0)/p_0$. There are three distinct regimes of cylindrical shockwave strength that we may compare to, Lin’s strong shock, Plooster’s intermediate, and general weak shock theory. Finding the maximum pressure in the simulation domain we may calculate the overpressure as both a function of space and time. Figure 41 shows points calculated from our simulation suite at 50 nanoseconds spacing plotted as a function of normalized radius r/R_0 where R_0 is dependent on ambient medium properties: $R_0 \equiv \dfrac{E_0/h}{b\gamma p_0}$ where b is a material dependent parameter[56], γ the usual ratio of specific heats which is here fixed, p_0 is the ambient pressure, and E_0/h the line energy density deposited into the channel. We note that all the simulations start at the strong shock solution, but quickly diverge from the strong shock to Plooster’s intermediate solution which bridges the strong and weak solutions. At the end of the simulation at $\approx 3\mu s$ the observed shocks from the simulations are still in the intermediate shock regime. The weak shock regime is not observed.

One reason to classify the shocks seen in these ESD events as strong, intermediate, or weak is to leverage that knowledge to futher reduce analytic models of the discharge. The strong shock regimes is of particular interest to the value of the Rankine-Hugoniot jump conditions (used by Lin in his similarity solution analysis [51]). We may quantify the strong shock regime by noting that at early times the strong shock has not yet had time to form, Figs. 38 and 40, the time of formation maximally being 50 ns, from Fig. 41. Departure from the strong shock regime may be arbitrarily calculated when the strong shock value is 5% different that the recorded overpressure value. Table II shows departure results for all four experimentally validated simulations.

[§§] When one derives the shock jump conditions from the Euler equations the pressure p and flow velocity u across an “interface”/piston are equal, leaving mass density ρ as a varying quantity [52]. At the shockfront the usual Rankine-Hugoniot are used and all three variables may vary. There are only three variables if a definite equation of state is used to reduce the specific internal energy to solely a function of mass density and pressure.

[¶¶] The initiation of the discharge in our simulations is simply when we begin to run the simulation. However, the “start of current” or initiation in the experiment is rather harder to pin down, see Table I.

[***] On the other hand the question of sonic connection between the channel and the shockwave is another matter.

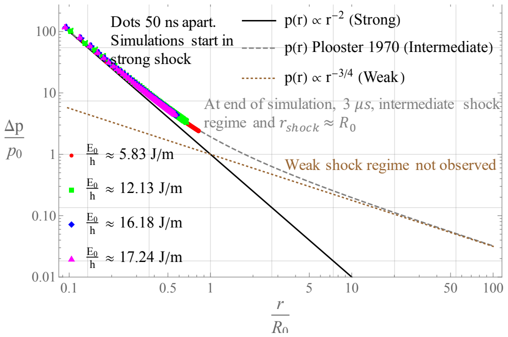

Fig. 41: Overpressure, $\frac{\Delta p}{p_0}$, plotted as a function of normalized radial coordinate. The strong, intermediate, and weak shock regimes in cylindrical geometry are plotted and compared to the experimentally-validated, theoretically-verified simulation data for the four experiments.

TABLE II: Table showing the domain of the strong shock regime.

Shot #	E_0/h (J/m)	R_0 (µm)	R_{sep} μm@(ns)
1	5.83	3,640	680@250
2	12.13	5,210	970@275
3	16.18	6,020	1,120@312
4	17.24	6,210	1,150@320

With this knowledge we may begin to develop further reductionist models to assist in the development of the ESD simulation toolset. The domain of applicability of the strong shock solutions may be solidly regarded then as $\{\sim \lambda_R, \sim 50 \text{ ns}\} \to \{\sim 10000 \text{ µm}, 100\text{s ns}\}$.

D. Energy Budget Calculation

Using the results of the above validation and verification we may quantify one of the metrics of interest detailed in this report. The amount of energy *guaranteed* to not be going into the victim load through by the hydrodynamic energy terminus, Fig. 3. Using the fitted terms from the strong shock radial solution we were able to obtain guesses for the energy deposited per unit length into the channel E_0/h. Multiplying this number by the length of the channel (6.28 mm) we were able to obtain the amount of energy going into the shockwave. Table III shows summary results of this calculation.

TABLE III: Table showing the amount of energy going in the hydrodynamics, energy stored on the initial object, and then hydrodynamic energy percentage.

Shot #	E_0/h (J/m)	$CV^2/2$ (mJ)	E_0 (mJ)	Hydro%
1	5.83	112.5	36.6	32.5
2	12.13	200.0	76.1	38.1
3	16.18	312.5	101.5	32.5
4	17.24	312.5	108.1	34.6

Further details regarding how much energy is guaranteed to go into the hydrodynamics may be found in an unpublished LANL technical report by Pocher, Murphy, Rose, Morgan, Peery, and Mace [13].

E. Capacitive Discharge Coupling

Since we now have an experimentally validated, Section V-B, theoretically verified, Section V-C, simulation suite based on the hydrodynamics, we may now combine it with other physics, namely a capacitive discharge code. A three level H system detailed in Section III-A2 is used in order populate the chemical kinetics, while the capacitive circuit model (no inductor $L = 0$) described in **??** III-A1b is used. An operator splitting method is used to separate the hydrodynamics, plasma kinetics, and the circuit variables. The initial condition used in the code has the capacitor charged to an initial voltage of $V(0) = V_0$ holding charge $Q(0) = Q_0$, with zero current $I(0) = 0$. The plasma kinetic variables hold the initial condition of Gaussians in space similar to the empirical heat source term used earlier in the report. The hydrodynamics variables are all set to quiescent, ambient conditions. Operator splitting takes the form of solving first the hydrodynamics explicitly, then also solving *explicitly*[†††] the plasma kinetics and circuit variables.

Since the chemical kinetics and circuit model are all ODEs that may be solved without recourse to the hydrodynamics. They are solved individually on a cell-by-cell basis. Each cell in the Lagrangian hydro code essentially becomes its own little dynamical system whose evolution is determined by local thermodynamic conditions.

Initial results from running this code show some promise, however, there is a fly in the ointment. Due to the size of the timesteps required in order to run the simulations to completion, it is computationally expensive to run the simulations with requisite resolution resolving kinetics and circuit variables. For example, the required timesteps are on order of 10,000/10^4 times smaller than the timesteps required for the hydrodynamics! To put this into perspective, consider walking a mile. For a healthy adult this should take about 20 minutes. Now consider walking a mile, but you can only take 1 meter a step, and that you can only step once every second. It would be slightly annoying, but again a healthy adult could do this easily. Now consider being told you can only take once centimeter a step, then only 0.1 mm a step. It would take someone 44 hours and ~4,000 hours to complete these two different tasks. This the analogy for our explicit code solver.

However, there are ways to remediate this issue; namely implicit solvers which allow larger timesteps. We may uncover the timescales of appropriate timesteps by analyzing the Jacobian matrix as done in Section III-D.

[†††] There are consequences, namely the size of stable timesteps, to solving these equations with the same explicit numerical operator as the hydrodynamics.

1) Stiffness of Differential Systems: A differential system is regarded as *stiff* if the timestep to solve the autonomous differential system is extremely small [57]. One way to find appropriate timescales/timesteps for numerical is to look at the eigenvalues λ_γ of the Jacobian matrix $J_{\alpha\beta} = \partial f_\alpha(\vec{\psi})/\partial\psi_\beta$ of the differential system of ODEs where ψ_α is the α'th variable, f_α is the evolution equation for variable ψ_α which is a function of all variables $\vec{\psi} \equiv [\psi_1 ... \psi_{n_s}]^T$ where n_s is the total number of dependent variables.

The differential system we analyze is the plasma kinetic and capacitive circuit discharge where we observe stiff numerical results in our total ESD toolset. The variable $\psi \in \{N_1, N_2, N_i, T_e, T_g, Q\}$ is the total phase space Γ, with $\{N_1, N_2, N_i\}$ being the compositional phase space Γ_C, and $\{T_e, T_g, Q\}$ being the plasma phase space Γ_P. Starting from generic initial conditions: $N_1 = N_0(1-2.0\text{e}-8), N_2 = 1.0\text{e}-8N_0, N_i = 1.0\text{e}-8N_0, T_e = 300\text{ K}, T_g = 300\text{ K}, Q = Q_0$ with $N_0 = 2.5\text{e}25$ (1/m^3) and $Q_0 = 2$ µC. Solving this equation as a function of time and plugging in the trajectories from phase space Γ into the Jacobian matrix we may obtain the eigenvalues $\lambda_\gamma(t)$, see Fig. 42. The eigenvalues give an indication as how quickly “information" is exchanged among the characteristic variables.

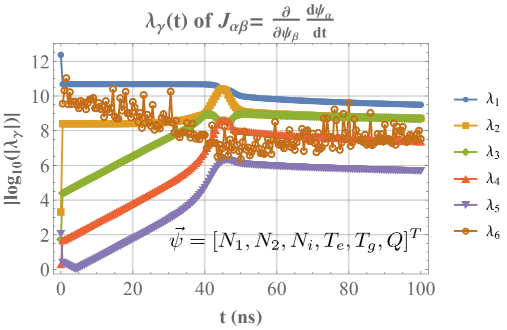

Fig. 42: Eigenvalues of the Jacobian matrix, $J_{\alpha\beta}$, of the capacitive differential system. The plot shows the absolute value of the logarithm of the absolute value of λ_γ. Note the disparate orders of magnitude. The noisy, brown dotted line is a zero eigenvalue arising from conservation of total particle number N_0.

The disparate orders of magnitude that are evident from Fig. 42 give credit to the observation that the the ESD evolution toolset has a numerically stiff system. The system we are analyzing right now is solely the plasma kinetic and circuit differential system that is solved on a cell by cell basis in the current formulation of the ESD evolution toolset. If the full differential system of the hydrodynamic code was included to the magnitudes of those eigenvalues would be much less than than already shown.

We may further take a ratio $r_{\gamma\delta} \equiv \lambda_\gamma/\lambda_\delta$ of the eigenvalues to determine the stiffness ratio of this subset differential system, see Fig. 43. The stiffness ratio informs us as to the relative size of appropriate timesteps so that the solution is not numerically unstable.

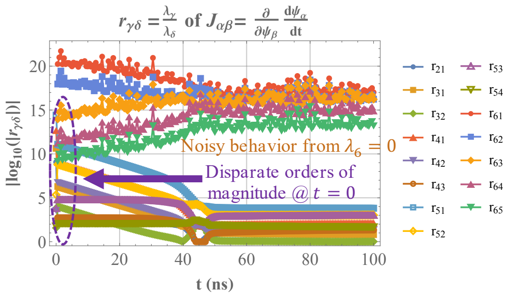

Fig. 43: All 15 eigenvalue ratios: $r_{\gamma\delta} \equiv \lambda_\gamma/\lambda_\delta$ of the Jacobian matrix, $J_{\alpha\beta}$. The disparate orders of magnitude shows that an extremely small timestep is needed to ensure numerical stability.

The ratios plotted in Fig. 43 show explicitly that the subset differential system of the plasma kinetic and circuit variables require an implicit solver to be computationally feasible. An implicit solver will allow a numerical operator to take larger, and more computationally tractable, timesteps. Using this knowledge gleaned from our physical analysis we may propose a physically motivated evolution of the numerical operators used for the ESD toolset.

F. A Physically Motivated Numerical Operator

An explicit numerical scheme that treats hydrodynamics, plasmas kinetics, and circuit variables equivalently has been shown to be computationally infeasible. Our detailed analysis of the (stiff) eigenvalue ratios has indicated that an explicit time scheme is not practical. A different numerical operator that reflects the needs of the time scales of the differential system needs to be used. This physically motivated numerical operator is a implicit time solver.

We propose that the physically motivated implicit time solver be used for the plasma kinetic and the circuit variables that are solved on a individual cell-by-cell basis. This implicit solver would be a constituent component of the entire ESD toolset. A proposed evolution of the ESD toolset may be seen in Fig. 44 [19]. The current module that was completed in the summer of 2021 has currently a totally explicit temporal numerical operator. The proposed evolution breaks up the three constituent physics (hydrodynamics, plasma kinetics, and capacitive circuit) making up the solved ESD event in the capacitive discharge simulations into modular sections. Each physics module will have a solver that would meet its own temporal timestep stability needs.

VI. DISCUSSION

In conclusion, throughout this report we have showcased the following:

- Performed detailed analysis into chemical kinetics providing insight into underlying dominant physical scales:

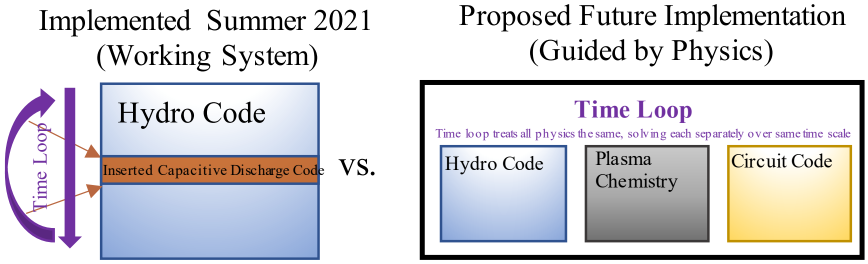

Fig. 44: Current and proposed evolution of the ESD simulation toolset.

species, timescales, and species interaction. For low temperature kT_e the dominant species is ground N_1. As the temperature increases the ionized species N_i becomes dominant with the dominance tradeoff occurring at approximately 2 eV. For higher numbers of ionized species the excited species "eat away" at the total equilibrium number of the ionized species at moderate temperature $\approx$ 2 eV, however at higher temperature > 4 eV the ionized species regains its marked dominance. The timescales of equilibration based Lyapunov functions $V_{\widetilde{\eta}}$ do not vary much as a function of the total species in our analyzed models. The timescale for equilibration for temperature < 1.5 eV is on the order of $\tau^{(eq)} \sim$ µs, while for $>$ 2.5 eV the equilibration time is on the order of ns. As noted in our analysis the Jacobian matrix, we showed that the dominant interaction for most species is with either the ionized species N_i/η_i or it nearest excited neighbor $N_{\alpha\pm1}/\eta_{\alpha\pm1}$.

- Showcased potential of model reduction methods and proposed viable extension. The ILDM method has been shown to have a working proof of concept to uncover the slow manifold characteristic of the chemical kinetic simulations. We also enumerated alternative dimension reduction schemes such as the statistical physics motivated method Boltzmann grouping of of vibrational levels or PCA analysis of trajectories in the composition space Γ_C.
- Substantiated and quantified the applicable space-time domain for Lin's strong shock limit. The domain of applicability (recall $\{\sim \lambda_R, \sim 50\text{ ns}\} \rightarrow \{\sim 10000\ \mu\text{m}, 100\text{s ns}\}$) for the strong shock limit in cylindrical geometry has been shown from an experimentally validated and and theoretically verified simulation suite. This includes quantifying the density profile evolution and overpressure calculation as a function of a normalized radius measurement.
- Theoretically verified and experimentally validated energy "earmarked" for hydrodynamic advection. Quantified the percentage of energy going into the ESD energy budget [13]. Around 30% of the energy stored on the capacitor in Michael Murphy's and Doug McHugh's legacy experiments has been shown to be sunk into the hydrodynamic energy terminus, an energy sink in the ESD energy flow network. This is a conservative estimate of the total energy that is available to flow through the spark to other circuit components.
- Developed understanding of constituent ESD physics and proposed physics-motivated generation of general ESD toolset. The physics motivating this evolution is based on the stiffness of the differential systems constituting the dynamical system that is solved on a cell by cell basis throughout the hydrodynamic framework. The proposed numerical operator will be dependent on the timescales of the physics to ensure numerical timestep stability.

ACKNOWLEDGMENTS

The authors wish to thank the Weapons Division at Los Alamos National Laboratory (LANL) for their overall support of this project and in specific the management of W-10. We also wish to thank Nathaniel Morgan, Jacob Moore, and Vincent Chiravelle, creators of the Fierro code, without which our hydrodynamic simulations would not have been possible. The experimental data collected by Doug Tasker, along with the legacy data of Dough McHugh and Michael Murphy were all vitally important to the success of this effort. Finally, the authors wish to thank Laura Cartelli and Francis Martinez for their expert advice and feedback.

REFERENCES

[1] J. Rose, M. Coffey, P. Flammer, M. LaCount, L. Pocher, C. Schrama, D. Borovina, J. Mace, and C. Durfee, "Finite Element Modeling of Electrostatic Discharge Using a Collisional Plasma Spark Conductivity Model," *Bulletin of the American Physical Society*, vol. 62, 2017.

[2] J. W. Rose, M. Lacount, L. Pocher, M. Coffey, P. D. Flammer, and C. Durfee, "Year 1 Report: Computational Study of Electrostatic Discharge," Colorado School of Mines, Tech. Rep., 2017.

[3] J. W. Rose, L. Pocher, C. Schrama, P. D. Flammer, and C. Durfee, "ESD Modeling Project: Year 2+ Report," Colorado School of Mines, Tech. Rep., 2018.

[4] J. W. Rose, C. A. Schrama, S. C. Hinnegan, J. Barolak, G. Shchedrini, D. E. Adams, P. D. Flammer, and C. G. Durfee, "Annual Report: Electrostatic Discharge Physics," Colorado School of Mines, Tech. Rep., 2019.

[5] C. Schrama, *Electric Field Sensing through Second Harmonic Generation of Ultrafast Laser Pulses*. Colorado School of Mines, 2018.

[6] J. W. Rose, M. W. Coffey, P. D. Flammer, T. B. Peery, J. L. Mace, and C. Durfee, "Nonlinear Spark Resistance and Capacitive Circuit Models of Electrostatic Discharge," *IEEE Transactions on Plasma Science*, vol. 48, no. 2, pp. 462–470, 2020.

[7] C. Schrama, S. Hinnegan, J. Rose, J. Davis, P. D. Flammer, and C. Durfee, "Measuring Time Dependence of Channel Resistance for Threshold Electrostatic Discharge," *Bulletin of the American Physical Society*, vol. 66, 2021.

[8] P. Flammer, J. Rose, C. Schrama, J. Mace, and C. Durfee, "Closed-Form Equilibrium Solution to Boltzmann Equation for Charged Particles in Electric Field," *Bulletin of the American Physical Society*, vol. 66, 2021.

[9] J. Rose, M. Zammit, J. Jung, A. Neukirch, C. Schrama, L. Pocher, T. Peery, J. Colgan, C. Durfee, and J. Mace, "Kinetic Models of ESD Spark Resistance in Atmospheric Pressure Gases," *Bulletin of the American Physical Society*, vol. 66, 2021.

[10] J. Barolak, C. Schrama, C. Durfee, and D. Adams, "Single-Shot Ptychography as a Diagnostic Imaging Technique for Studying Electro-Static Discharge," *Bulletin of the American Physical Society*, vol. 66, 2021.

[11] F. N. Doherty, *Radial Gerchberg-Saxton Algorithm for Phase Retrieval and Spatial Flat-Top Beam Shaping of Azimuthally Symmetric Laser Beams*, 2021.

[12] J. W. Rose, L. A. Pocher, and D. T. A. Haynes, "Simulation of Electrostatic Discharge," August 2019.

[13] L. A. Pocher, M. J. Murphy, J. W. Rose, N. R. Morgan, T. B. Peery, and J. L. Mace, "On Hydrodynamics Generated from Electrostatic Discharges: A Heat Source Perspective," Los Alamos National Lab.(LANL), Los Alamos, NM (United States), Tech. Rep., 2020.

[14] L. A. Pocher, "Direct E&M Field Solver for a Plane Wave without Sources," Los Alamos National Laboratory (LANL), Los Alamos, NM (United States), Tech. Rep., 2020.

[15] L. A. Pocher, N. R. Morgan, T. B. Peery, and J. L. Mace, "Analysis into Asymptotic Convergence to Full Nonlinear Solutions and Exploration of the Implication of Numerical Operator Mutation of Differential Systems," Los Alamos National Laboratory (LANL), Los Alamos, NM (United States), Tech. Rep., 2020.

[16] ——, "Implications of Numerical Operator Mutation on Differential Forms: Locally Negative Entropy Production," August 2020.

[17] ——, "Exploration of the Implication of Numerical Operator Mutation of Differential Systems," in *International Mechanical Engineering Congress & Exposition Abstracts*, 2020.

[18] ——, "Asymptotic Convergence to a Full Nonlinear Solution," in *APS Division of Fluid Dynamics Meeting Abstracts*, 2020, pp. W12–002.

[19] L. A. Pocher, J. W. Rose, T. B. Peery, and J. L. Mace, "Physics Guided Simulation of Electrostatic Discharge," September 2021, 1st LANL ESD-WRI Symposium.

[20] L. A. Pocher, M. J. Murphy, J. W. Rose, N. R. Morgan, T. B. Peery, and J. L. Mace, "Joule Heating Driving Hydrodynamic Explosions from an Electrostatic Discharge Event," in *APS Division of Fluid Dynamics*, 2021.

[21] V. Chiravalle and N. Morgan, "A 3D finite element ALE method using an approximate Riemann solution," *International Journal for Numerical Methods in Fluids*, vol. 83, no. 8, pp. 642–663, 2017.

[22] N. R. Morgan, K. N. Lipnikov, D. E. Burton, and M. A. Kenamond, "A Lagrangian staggered grid Godunov-like approach for hydrodynamics," *Journal of Computational Physics*, vol. 259, pp. 568–597, 2014.

[23] D. A. Xu, D. A. Lacoste, D. L. Rusterholtz, P.-Q. Elias, G. D. Stancu, and C. O. Laux, "Experimental study of the hydrodynamic expansion following a nanosecond repetitively pulsed discharge in air," *Applied Physics Letters*, vol. 99, no. 12, p. 121502, 2011.

[24] D. Xu, M. Shneider, D. Lacoste, and C. Laux, "Thermal and hydrodynamic effects of nanosecond discharges in atmospheric pressure air," *Journal of Physics D: Applied Physics*, vol. 47, no. 23, p. 235202, 2014.

[25] Y. Ling and S. Balachandar, "Asymptotic Scaling Laws and Semi-Similarity Solutions for a Finite-Source Spherical Blast Wave," *Journal of Fluid Mechanics*, vol. 850, pp. 674–707, 2018.

[26] S. I. Braginskii, "Theory of the development of a spark channel," *Sov. Phys. JETP*, vol. 34, pp. 1068–1074, 1958.

[27] V. Rojansky, *Electromagnetic Fields and Waves*. New York: Dover, 1979.

[28] Yu. P. Raizer, *Gas Discharge Physics*. Berlin: Springer, 1991.

[29] L. Vriens and A. H. M. Smeets, "Cross-section and rate formulas for electron-impact ionization, excitation, deexcitation, and total depopulation of excited atoms," *Physical Review A*, vol. 22, no. 3, pp. 940–951, 1980.

[30] L. C. Johnson, "Approximations for collisional and radiative transition rates in atomic hydrogen," *The Astrophysical Journal*, vol. 174, pp. 227–236, 1972.

[31] Y. B. Zel'Dovich and Y. P. Raizer, *Physics of Shock Waves and High-Temperature Hydrodynamic Phenomena*. Courier Corporation, 2012.

[32] L. L. Alves, A. Bogaerts, V. Guerra, and M. M. Turner, "Foundations of modelling nonequilibrium low-temperature plasma," *Plasma Sources Science and Technology*, vol. 27, p. 023002, 2018.

[33] S. Wiggins, *Introduction to Applied Nonlinear Dynamical Systems and Chaos*. Springer-Verlag, 1990.

[34] L. E. Reichl, *A Modern Course in Statistical Physics*. University of Texas Press, 1980.

[35] E. Ott, *Chaos in Dynamical Systems*, 2nd ed. Cambridge University Press, 2002.

[36] U. Maas and S. B. Pope, "Simplifying Chemical Kinetics: Intrinsic Low-Dimensional Manifolds in Composition Space," *Combustion and flame*, vol. 88, no. 3-4, pp. 239–264, 1992.

[37] U. Maas, "Efficient calculation of intrinsic low-dimensional manifolds for the simplification of chemical kinetics," *Computing and Visualization in Science*, vol. 1, no. 2, pp. 69–81, 1998.

[38] S. Borok, I. Goldfarb, V. Gol'dshtein, and U. Maas, ""Ghost" ILDM-Manifolds and Their Identification," in *Model Reduction and Coarse-Graining Approaches for Multiscale Phenomena*. Springer, 2006, pp. 55–79.

[39] V. Bykov and U. Maas, "The extension of the ILDM concept to reaction–diffusion manifolds," *Combustion Theory and Modelling*, vol. 11, no. 6, pp. 839–862, 2007.

[40] A. N. Gorban, "Model reduction in chemical dynamics: slow invariant manifolds, singular perturbations, thermodynamic estimates, and analysis of reaction graph," *Current Opinion in Chemical Engineering*, vol. 21, pp. 48–59, 2018.

[41] A. Gorban and I. Karlin, "Hilbert's 6th problem: exact and approximate hydrodynamic manifolds for kinetic equations," *Bulletin of the American Mathematical Society*, vol. 51, no. 2, pp. 187–246, 2014.

[42] A. Berthelot and A. Bogaerts, "Modeling of plasma-based CO2 conversion: lumping of the vibrational levels," *Plasma Sources Science and Technology*, vol. 25, no. 4, p. 045022, 2016.

[43] H. P. Le, A. R. Karagozian, and J.-L. Cambier, "Complexity reduction of collisional-radiative kinetics for atomic plasma," *Physics of Plasmas*, vol. 20, no. 12, p. 123304, 2013.

[44] A. Bellemans, T. Magin, A. Coussement, and A. Parente, "Reduced-order kinetic plasma models using principal component analysis: Model formulation and manifold sensitivity," *Physical Review Fluids*, vol. 2, no. 7, p. 073201, 2017.

[45] K. Peerenboom, A. Parente, T. Kozák, A. Bogaerts, and G. Degrez, "Dimension reduction of non-equilibrium plasma kinetic models using principal component analysis," *Plasma Sources Science and Technology*, vol. 24, no. 2, p. 025004, 2015.

[46] P. Bayle, M. Bayle, and G. Forn, "Neutral heating in glow to spark transition in air and nitrogen," *Journal of Physics D: Applied Physics*, vol. 18, no. 12, p. 2395, 1985.

[47] F. Tholin and A. Bourdon, "Simulation of the hydrodynamic expansion following a nanosecond pulsed spark discharge in air at atmospheric pressure," *Journal of Physics D: Applied Physics*, vol. 46, no. 36, p. 365205, 2013.

[48] S. Tzortzakis, B. Prade, M. Franco, A. Mysyrowicz, S. Hüller, and P. Mora, "Femtosecond laser-guided electric discharge in air," *Physical Review E*, vol. 64, no. 5, p. 057401, 2001.

[49] M. Murphy and S. A. Clarke, "Simultaneous photonic doppler velocimetry and ultra-high speed imaging techniques to characterize the pressure output of detonators," in *AIP Conference Proceedings*, vol. 1426, no. 1. American Institute of Physics, 2012, pp. 402–405.

[50] M. J. Murphy, M. A. Lieber, and M. M. Biss, "Novel Measurements of Shock Pressure Decay in PMMA Using Detonator Loading," in *AIP Conference Proceedings*, vol. 1979, no. 1. AIP Publishing LLC, 2018, p. 160020.

[51] S.-C. Lin, "Cylindrical Shock Waves Produced by Instantaneous Energy Release," *Journal of Applied Physics*, vol. 25, no. 1, pp. 54–57, 1954.

[52] G. B. Whitham, *Linear and Nonlinear Waves*. John Wiley & Sons, 2011, vol. 42.

[53] L. Landau and E. Lifshitz, *Fluid Mechanics*. Oxford, 1982.

[54] R. Courant and K. O. Friedrichs, *Supersonic Flow and Shock Waves*. Springer Ccience & Business Media, 1999, vol. 21.

[55] M. N. Plooster, "Shock Waves from Line Sources. Numerical Solutions and Experimental Measurements," *The Physics of Fluids*, vol. 13, no. 11, pp. 2665–2675, 1970.

[56] D. Jones, "The energy parameter b for strong blast waves," Tech. Rep., 1962.

[57] G. Dahlquist and A. Bjorck, "Numerical Methods (transl. by N. Anderson)," 1974.